J. Fluid Mech. (2000), *vol.* 424, *pp.* 327–365. Printed in the United Kingdom

Sound generation by coaxial collision of two vortex rings

By O. INOUE, Y. HATTORI AND T. SASAKI

Institute of Fluid Science, Tohoku University, 2-1-1 Katahira, Aoba-ku, Sendai 980-8577, Japan

(Received 9 December 1998 and in revised form 6 June 2000)

Sound pressure fields generated by coaxial collisions of two vortex rings with equal/unequal strengths are simulated numerically. The axisymmetric, unsteady, compressible Navier–Stokes equations are solved by a finite difference method, not only for a near field but also for a far field. The sixth-order-accurate compact Padé scheme is used for spatial derivatives, together with the fourth-order-accurate Runge–Kutta scheme for time integration. The results show that the generation of sound is closely related to the change of direction of the vortex ring motion induced by the mutual interaction of the two vortex rings. For the case of equal strength (head-on collision), the change of direction is associated with stretching of the vortex rings. Generated sound waves consist of compression parts and rarefaction parts, and have a quadrupolar nature. For the case of unequal strengths, the two vortex rings pass through each other; the weaker vortex ring moves outside the stronger vortex ring which shows a loop motion. The number of generated waves depends on the relative strength of the two vortex rings. The sound pressure includes dipolar and octupolar components, in addition to monopolar and quadrupolar components which are observed for the case of a head-on collision.

1. Introduction

Interactions of vortex rings may be one of the most fundamental mechanisms of sound generation in three-dimensional vortical flows. The interactions are observed in a round jet under certain conditions and are considered to play important roles in the generation of jet sound (Hussain & Zaman 1980; Zaman 1985; Shariff & Leonard 1992). Studies of sound generated by interactions of two vortex rings have been done for coaxial as well as oblique collisions both experimentally (Kambe & Minota 1983; Minota & Kambe 1986; Kambe, Minota & Takaoka 1993) and computationally (Shariff *et al.* 1988; Kambe *et al.* 1993; Tang & Ko 1995; Inoue & Hattori 1997; Adachi, Ishii & Kambe 1997; Ishii, Maru & Adachi 1997). In most of the studies, except for Tang & Ko (1995), two vortex rings of equal strength were considered.

Depending on the sense of rotation, coaxial interactions of two vortex rings can be divided into two categories: passage interactions and collision interactions (Shariff & Leonard 1992). In passage interactions, two vortex rings have the same sense of rotation, and travel in the same direction. The rear vortex ring attempts to pass through the front one, resulting in various patterns of vortex motion such as leapfrogging and merging. Passage interactions are observed in a round jet under certain conditions (Hussain & Zaman 1980; Zaman 1985). On the other hand, in collision interactions, two vortex rings have opposite senses of rotation, and travel toward each other. The radii of the vortex rings grow due to mutual induction. Collision interactions

are rarely observed in engineering applications, but interactions of vortex rings with opposite senses of rotation are observed in coaxial jets and are considered to play an important role in the generation of coaxial jet noise (Tang & Ko 1992, 1994).

Head-on collisions have been used by Kambe and his co-workers primarily to test theories of vortex sound generation. Using a microphone, Kambe & Minota (1983) and Minota & Kambe (1986) measured the pressure signals generated by the head-on collision of two vortex rings. Analysis of the observed signals showed that the acoustic pressure is composed of quadrupolar and monopolar components. They compared the measured data with the values predicted by an inviscid theory and also by a viscous theory. The inviscid theory failed to predict either the appearance of the monopole or the behaviour of the quadrupole in the later stage of evolution. On the other hand, the viscous theory predicted the appearance of the monopole and described the evolution of the quadrupole much better than the inviscid theory. The results of Minota & Kambe suggest that the viscous effect may not be negligible in sound generation, though the computational results of Shariff *et al.* (1988) showed that inviscid core deformation is sufficient to explain the later stage of quadrupole evolution. So far few experimental studies have been done on sound generated by the collision of vortex rings.

In computational analyses of vortex sounds, numerical simulations are often separated into two parts: the aerodynamic part and the acoustic part (Kambe *et al.* 1993; Ishii *et al.* 1997). First, in the aerodynamic part, near-field flow structures of vortex interactions are obtained by simulating the flow field: for example, by the (incompressible) Navier–Stokes simulations (Kambe *et al.* 1993; Adachi *et al.* 1997; Ishii *et al.* 1997) or by inviscid contour dynamics methods (Shariff *et al.* 1988; Tang & Ko 1995). Then, in the acoustic part, the far-field sound pressure is calculated theoretically, using the near-field flow quantities obtained in the aerodynamic part. This method saves computational time as well as memory storage compared with direct numerical simulations, because the flow in the far field is assumed to be still or uniform and thus is not solved for numerically.

Kambe *et al.* (1993) studied sounds generated by the oblique collision of two vortex rings at right angles both computationally and experimentally. The three-dimensional, incompressible, Navier–Stokes equations were solved by a pseudo-spectral method. The evolution of the vorticity field obtained was used to predict the sound pressure wave by using a theoretically derived formula. Independently, a laboratory experiment was performed using a shock tube (the Mach number was 0.08). The wave modes obtained from the laboratory experiment and the computer simulation were compared. Both results are in qualitative agreement, and show the appearance of octupolar components in addition to the quadrupolar components.

Using a contour dynamics method, Shariff *et al.* (1988) studied flow fields produced by head-on collision and by the passage interaction of two vortex rings. The far-field acoustic sound was calculated using the theory of Kambe & Minota (1983). For the case of head-on collision, a contour dynamics result for thick vortex rings showed good overall agreement with the experiment of Kambe & Minota (1983). For the case of passage interaction, the results showed wavy oscillations of the sound pressure which may be related to core deformations. Also using a contour dynamics method, Tang & Ko (1995) studied an axisymmetric, incompressible, inviscid flow field produced by the collision of two vortex rings with equal/unequal strengths. The corresponding far-field sound pressure was calculated using the formula of Möhring (1978). They found that the vortex ring dynamics and the sound generation mechanism depend significantly on the strength (circulation) ratio of the two colliding vortex rings.

Adachi *et al.* (1997) numerically studied sound generated by the oblique collision of two vortex rings at right angles. For the near-field vorticity region, the three-dimensional, incompressible Navier–Stokes equations were solved by a vorticity–potential method. The results were used to obtain the far-field sound pressure by using a theory formulated in the form of multipole expansions. The results were consistent with the experiment of Kambe *et al.* (1993), not only for the near-field vortex ring dynamics, but also for the far-field sound pressures. Though this type of computational method gives qualitatively similar results to experiments, the generation process and the propagation process of the sound in the near and transition fields are not seen directly by this method.

A new development has been the field of computational aeroacoustics (CAA), where both the fluid motion and the sound which it generates are directly computed (Colonius, Lele & Moin 1994, 1997; Mitchell, Lele & Moin 1995; Inoue & Hattori 1999). For comprehensive reviews, readers are referred to Tam (1995), Lele (1997) and Moin & Mahesh (1998). In these simulations, the Navier–Stokes equations were solved by using highly accurate schemes both for space and time in order to precisely capture the sound pressure, which is usually much smaller than the pressure in the near-field fluid flow. As noted by Moin & Mahesh (1998), CAA is still in its infancy, and there are many problems remaining to be studied using it.

The purpose of this paper is to study, using direct Navier–Stokes simulations (DNS), the generation and propagation mechanisms of the sound in an axisymmetric flow field produced by coaxial collisions of two vortex rings with equal/unequal strengths and to increase our understanding of the characteristic features of the sound. First, we examine the basic nature of the sound generated by the head-on collision of two vortex rings, which is one of the most simplified models of three-dimensional vortical flows. Special attention is paid to the relation between the vortex ring dynamics and the sound pressure it generates. The effects of the Mach number of the vortex rings and the Reynolds number are also examined. The sound pressure signals are compared with the experiment of Minota & Kambe (1986). Then, as an example of more complex cases, we simulate the flow field produced by the collision of two vortex rings with unequal strengths and examine the effects of the inequality on sound generation.

2. Direct Navier–Stokes Simulation

2.1. *Mathematical formulation and numerical procedure*

2.1.1. *Flow model and parameters*

A schematic diagram of the flow model is presented in figure 1. We assume that the flow is axisymmetric with respect to the x-axis. The radial coordinate is expressed by y. Two vortex rings are set initially to move along the x-axis and collide with each other near the y-axis ($x = 0$). The vortex ring on the left-hand side (hereafter referred to as the left vortex ring) which moves from left to right is denoted by the subscript 1, and the vortex ring on the right-hand side (right vortex ring) which moves from right to left is denoted by the subscript 2. The symbol R_0 denotes the radius of the vortex rings, and R_c denotes the core radius. Both the ring radius and the core radius are assumed to be the same for the two vortex rings.

The vortex rings are assumed to have a Gaussian distribution of vorticity initially. For example, the initial distribution of the vorticity of the left vortex ring is

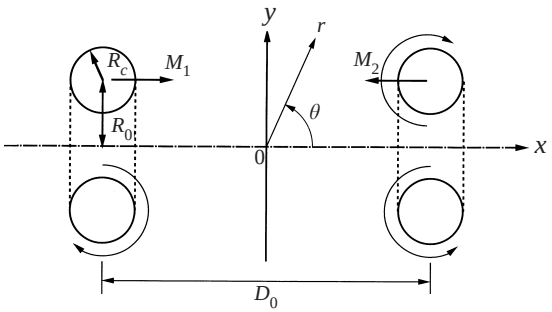

FIGURE 1. Schematic diagram of the flow model.

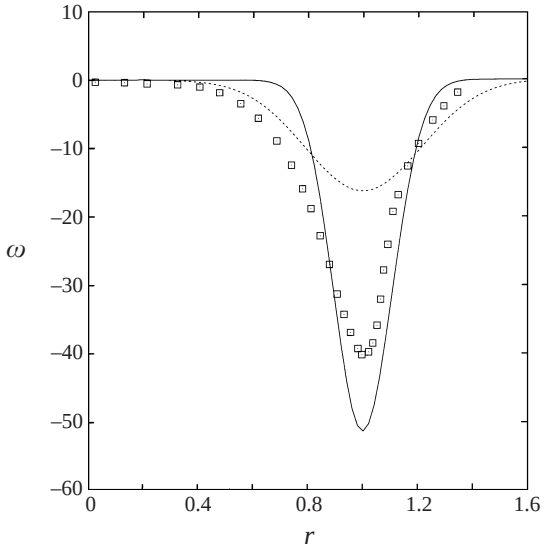

FIGURE 2. Initial distributions of the vorticity. ———, $r_c = 0.15$; – – – –, $r_c = 0.3$. □, Sullivan *et al.* (1973), $r_c = 0.24$.

expressed as

$$\omega_1(x, y) = \frac{\Gamma_1}{\pi R_c^2} \exp\left[-\frac{(x - x_1)^2 + (y - y_1)^2}{R_c^2}\right]. \tag{2.1}$$

The symbol Γ denotes the circulation, and (x_1, y_1) is the centre of the vortex core. The initial translational velocity of the vortex ring, U_1, is related to the circulation, Γ_1, by (Saffman 1970)

$$U_1 = \frac{\Gamma_1}{4\pi R_0}\left[\ln\left(\frac{8R_0}{R_c}\right) - 0.558\right]. \tag{2.2}$$

A similar relation holds for Γ_2 and U_2. For reference, the initial distributions of the vorticity for the cases of $r_c \equiv R_c/R_0 = 0.15$ and 0.3 are presented in figure 2, together with the experimental result of Sullivan, Widnall & Ezekiel (1973) for $r_c = 0.24$.

The Mach number of the left vortex ring, M_1, and that of the right vortex ring, M_2, are defined by $M_1 = U_1/c_\infty$ and $M_2 = U_2/c_\infty$, respectively. Here, the symbol c_∞ denotes the speed of sound. In this study, except for figures 18(e) and 18(f) shown later, we assume $M_1 \geqslant M_2$.

The lengths are made dimensionless by the vortex ring radius R_0. The velocity may be scaled either by U_1 or by c_∞. If we make the flow quantities dimensionless with U_1, the Reynolds number may be defined as $Re^* = U_1 R_0/\nu_\infty$, where ν is the kinematic viscosity. In this case, the time scale is unity. If we choose c_∞ as the characteristic velocity, instead of U_1, the Reynolds number may be defined as $Re = c_\infty R_0/\nu_\infty$, and the time scale is $1/M_1$. Another meaningful Reynolds number may be $Re^{**} = \Gamma_1/\nu_\infty$, which is based on the circulation Γ_1. As the sound pressure waves propagate at the speed of sound, the relation between the pressure signals observed in the transitional and far fields and the vortex ring motion in the near field which generates the signals may be more easily understood by the use of the time t which is based on the speed of sound. On the other hand, the vortex ring motion itself may be characterized by U_1. In addition, as will be seen later, several interesting features of the sound pressure (for example, figures 13, 27 and 28) are well illustrated by the time t^* which is based on U_1. The three Reynolds numbers are all related to each other, through equation (2.2), as

$$Re = Re^*/M_1 \tag{2.3}$$

$$= \frac{Re^{**}}{4\pi M_1}\left[\ln\left(\frac{8}{r_c}\right) - 0.558\right]. \tag{2.4}$$

The times t and t^* are also related to each other as

$$t^* = M_1 t. \tag{2.5}$$

In this study, the Reynolds numbers Re and Re^* and the times t and t^* are used together. The Reynolds number Re^{**} is also used where appropriate (for example, figure 15).

The Mach numbers are prescribed to be M_1, $M_2 = 0.075$ to 0.3. The Reynolds number prescribed is $Re^* = 150$ to 2000 ($Re = 1000$ to 13 300). The ratio of the core radius to the ring radius is prescribed to be either $r_c(\equiv R_c/R_0) = 0.15$ or 0.3. Since the Mach numbers are relatively low ($M_1, M_2 \leqslant 0.3$), temperature dependence of the transport properties is not likely to be a significant effect (Colonius *et al.* 1997). Therefore, the molecular viscosity and the thermal conductivity are taken to be constant. The Prandtl number is assumed to be 0.75, and the ratio of specific heats is 1.4.

2.1.2. *Numerical schemes and computational parameters*

The unsteady, axisymmetric, compressible Navier–Stokes equations are solved by a finite difference method. For spatial derivatives, a sixth-order-accurate compact Padé scheme (third-order-accurate at the boundaries) proposed by Lele (1992) is adopted. At the axis of symmetry, a fourth-order-accurate interpolation is used. The fourth-order Runge–Kutta scheme is used for time-integration. Non-reflecting boundary conditions (Poinsot & Lele 1992) are used at the boundaries.

A schematic diagram of the computational domain is presented in figure 3. According to the theory of low Mach number sound generation (for example, Goldstein 1976), the length scales are unity in the vortex region and $1/M_1$ in the sound region; the length scale in the sound region is larger than in the vortex region. The time scale is the same in the whole region: unity if the velocity is scaled by U_1 and $1/M_1$ if scaled by c_∞. Based on this estimation, we divide the computational domain into three regions of different grid spacings: a vortex region $[-x_v \leqslant x \leqslant x_v,\ 0 \leqslant y \leqslant y_v]$, a sound region $[-x_s \leqslant x \leqslant x_s, 0 \leqslant y \leqslant y_s]$, and a buffer region $[-x_b \leqslant x \leqslant x_b, 0 \leqslant y \leqslant y_b]$.

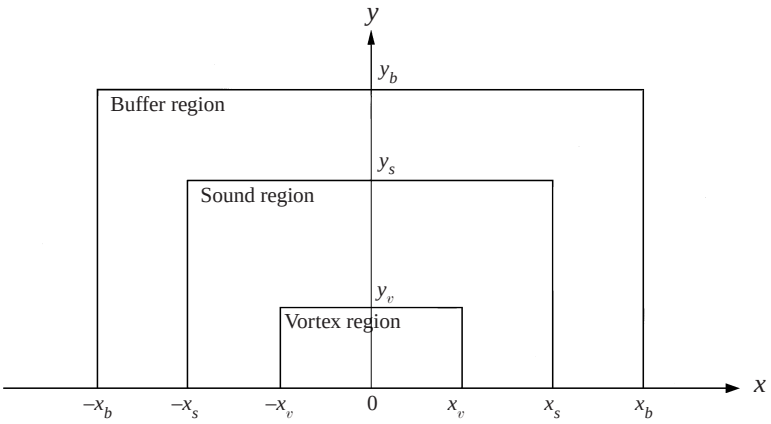

FIGURE 3. Schematic diagram of the computational domain.

The spacing in the vortex region is prescribed to be fine enough to capture the motion of vortex rings. In the sound region, the spacing is prescribed to be larger than that in the vortex region, but still small enough to capture sound pressure waves. The spacing in the buffer region is prescribed such that pressure waves damp with increase in distance and become sufficiently small before reaching the boundaries of the computational domain where the non-reflecting boundary conditions are used. The role of the buffer region is similar to that of the 'sponge region' of Colonius *et al.* (1997). Only the results obtained in the vortex region and in the sound region are used for analysis. The spacings among the three regions are connected smoothly by using a hyperbolic-tangent curve. In addition, we imposed a restriction that the increment of the spacing does not exceed 5%: $(\Delta x)_{i+1}/(\Delta x)_i \leqslant 1.05$.

The grid spacings and the sizes of each computational region were determined after many preliminary tests. The grid spacings are fixed to be $\Delta x_v = 0.02$, $\Delta x_s = 0.4$, and $\Delta x_b = 5.0$. The spacings in the y-direction are set equal to those in the x-direction: $\Delta y_v = \Delta x_v$, $\Delta y_s = \Delta x_s$, and $\Delta y_b = \Delta x_b$. As the length scale in the sound region is $1/M_1$, the corresponding grid spacing Δx_s^* based on this scale, obtained from $\Delta x_s^* = M_1 \Delta x_s = 0.4 M_1$, is 0.12 for $M_1 = 0.3$ and 0.03 for $M_1 = 0.075$.

The size of the sound region is fixed to be $x_s = y_s = 80.0$. On the length scale $1/M_1$, this value is equivalent to the size 24.0 for $M_1 = 0.3$ and 6.0 for $M_1 = 0.075$. The size of the buffer region is fixed to be $x_b = y_b = 180.0$.

The size of the vortex region is slightly different among the cases treated, because the vortex ring motion varies depending on the combinations of the Mach numbers, M_1 and M_2. The typical values are $x_v = 12.7$, $y_v = 7.0$. The number of grid points is, typically, 1967 (x-direction) $\times$ 713 (y-direction). The time step is $\Delta t = 0.01$; thus, $\Delta t^* = 0.003$ for $M_1 = 0.3$ and $\Delta t^* = 0.00075$ for $M_1 = 0.075$.

2.2. *Initial conditions*

With the vorticity distributions given by equation (2.1), the initial velocity field was prescribed by solving the following equations, under the assumption that the flow is incompressible, $\nabla \cdot \boldsymbol{v} = 0$:

$$\boldsymbol{v} = \nabla \times \boldsymbol{A}, \qquad \nabla^2 \boldsymbol{A} = -\omega. \tag{2.6}$$

The boundary conditions for the above Poisson equation were prescribed by a solution of power series, which are known to converge well at the far field and near the axis

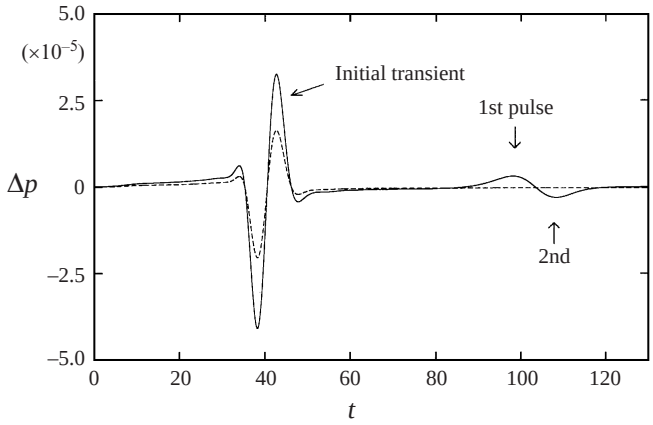

FIGURE 4. Time histories of the pressure measured at $r = 40$, $\theta = 90°$. $r_c = 0.15$, $Re = 3300$ ($Re^* = 500$). ———, Δp_c (two vortex rings with $M_1 = M_2 = 0.15$); – – – –, Δp_s (single vortex ring with $M_1 = 0.15$).

(Morse & Feshbach 1953). The assumption of incompressibility for the initial velocity field may be acceptable for sufficiently low Mach numbers. Once the velocity field is known, the initial density and pressure fields are determined by solving the Poisson equation

$$\nabla^2 \frac{p}{\rho} = -\frac{\gamma - 1}{\gamma} \frac{\partial u_i}{\partial x_j} \frac{\partial u_j}{\partial x_i}. \tag{2.7}$$

This equation is derived from the conservation of momentum under the assumption that the flow is steady, inviscid and homentropic: $p/\rho^\gamma = \text{const}$. Again, the far-field boundary conditions for this equation were prescribed by a solution of power series.

Though the Mach numbers treated in this study are relatively low ($M_1, M_2 \leqslant 0.3$), the initial flow field prescribed above is not the solution of the compressible Navier–Stokes equations. Therefore, at an early stage of the flow development, acoustic transients associated with the initial flow field are observed. A time history of the sound pressure, Δp_c, for the case of head-on collision with $M_1 = M_2 = 0.15$, $r_c = 0.15$, $Re = 3300$ ($Re^* = 500$), measured at $r = 40$ and $\theta = 90°$ is represented in figure 4 by the solid line; the dashed line is the pressure, Δp_s, for the case of a single vortex ring moving at its self-induced velocity. The modified pressure Δp is defined as $\Delta p = (p - p_\infty)$, where p_∞ denotes the ambient pressure. For the coordinate system (r, θ), see figure 1. As seen from figure 4, for the case of head-on collision, the initial transients are observed in the range $30 \leqslant t \leqslant 50$. The acoustic transients are observed not only for the case of head-on collision but also for the case of a single vortex ring; the initial transients for the single vortex ring are also observed in the same range $30 \leqslant t \leqslant 50$. No pressure waves except for the initial transients are observed for the single vortex ring. The initial locations of the two vortex rings are prescribed such that the collision occurs sufficiently after the acoustic transients pass through the vortex region; the first and the second pulses are observed after $t \geqslant 80$ in figure 4.

3. Results for two vortex rings of equal strength

In this section, computational results for the case of a head-on collision are presented. First, evolutions of the vortex ring motion and the sound pressure field are

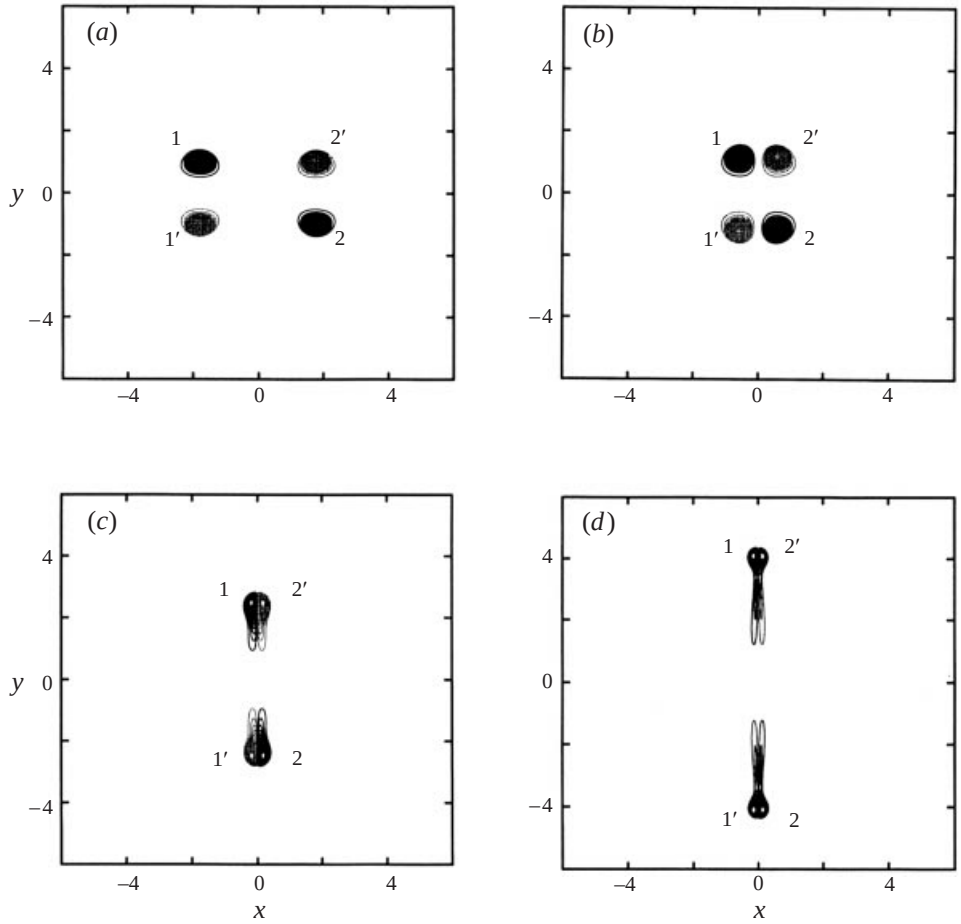

FIGURE 5. Time development of a vorticity field. $M_1 = M_2 = 0.15$, $r_c = 0.15$, $Re = 3300$ ($Re^* = 500$). The prime denotes clockwise rotation. The contour levels are from $\omega_{min} = -3.0$ to $\omega_{max} = 3.0$ with an increment of 0.1. (*a*) $t = 48$ ($t^* = 7.2$), (*b*) $t = 60$ ($t^* = 9.0$), (*c*) $t = 72$ ($t^* = 10.8$), (*d*) $t = 84$ ($t^* = 12.6$).

presented. It is shown that the generation of sound is related to the change of direction of the vortex ring motion associated with stretching. Then, the nature of the generated sound and the effects of the Mach number, the Reynolds number and the core radius are examined. It is shown that the generated sound waves consist of compression parts and rarefaction parts, and have a quadrupolar nature. The scaling law, $\Delta p \propto M_1^4/r$, which was predicted by Kambe & Minota (1983), is confirmed numerically. Then, the computational results are compared with the experiment of Minota & Kambe (1986) and the theoretical values predicted by an extended Möhring's method (Kambe & Minota 1983).

3.1. *Evolution of the vortex rings*

A typical example of a collision of two vortex rings of equal strength (head-on collision) is presented in terms of the vorticity in figure 5 for the case of $M_1 = M_2 = 0.15$, $r_c = 0.15$ and $Re = 3300$ ($Re^* = 500$). The figure shows the time development of the vorticity field in a meridional cross-section. The time is shown by t in the figure;

the corresponding time t^* is presented in the caption. The numbers 1 and 2 denote the left and right vortex rings, respectively, and the prime denotes clockwise rotation. The two vortex rings are initially located at $x = \pm 8.0$. With increased time, the two vortex rings approach along the x-axis until $t \sim 60$ (figure 5*a*, *b*), and then stretch in the direction perpendicular to the x-axis (figure 5*c*, *d*); the radii of the vortex rings grow with time. This series of events has been observed both in experiments (for example, Oshima 1978) and in computations (Shariff *et al.* 1988).

In a meridional cross-section of the flow field, the vortex rings behave as if they were vortex pairs in a two-dimensional flow. Thus, the explanation of the flow field in terms of the vortex pairs often makes it easy to understand the vortex ring motion. For example, the flow development shown in figure 5 can be explained as follows. Two vortex pairs, $(1, 1')$ and $(2, 2')$, approach along the x-axis initially at their respective self-induced velocities. With decrease in the distance between the two vortex rings, the mutual interactions between 1 and $2'$ and between $1'$ and 2 become stronger than those between 1 and $1'$ and between 2 and $2'$. As a result, the new vortex pairs, $(1, 2')$ and $(1', 2)$, move away from each other along the y-axis, resulting in stretching of the vortex rings. The explanation in terms of the vortex pair will be used frequently in this study.

3.2. *Generation and propagation of sound waves*

3.2.1. *Evolution of the pressure field near the vortex rings*

Isobars of $\Delta p\,(= p - p_\infty)$ around the vortex rings for the same case as in figure 5, are presented in figure 6. In the figures, the symbol $\oplus$ denotes the compression region where Δp is positive, and $\ominus$ denotes the rarefaction region where Δp is negative. When a single vortex ring moves at its self-induced velocity, the pressure in the neighbourhood of the core of that vortex ring becomes negative while that behind and ahead of the vortex ring becomes positive; in a meridional cross-section of the flow field, two rarefaction regions and two compression regions appear. Therefore, when two vortex rings move, as seen in figure 6(*a*), four rarefaction regions and four compression regions appear in a meridional cross-section of the flow field at an initial stage of the flow development. With increased time, the two vortex rings approach, and the compression regions ahead of the vortex rings merge, as seen near the origin in figures 6(*b*) and 6(*c*). Then, the vortex rings start to stretch at $t \sim 60$, and their radii grow with time.

As noted in the previous section, the new vortex pairs, $(1, 2')$ and $(1', 2)$, in the meridional cross-section move outward along the y-axis (figure 5*c*, *d*). This outward motion produces new compression regions ahead of the vortex pairs, which are marked by open arrows in figure 6(*d*). The appearance of the new compression regions forces the rarefaction regions around the vortex pairs to move circumferentially, as shown by solid arrows in figure 6(*d*). This circumferential movement of the rarefaction regions produces new rarefaction regions outside the compression regions near the x-axis, as seen in figure 6(*e*). The new compression regions (which are generated ahead of the outward moving vortex pairs) and the new rarefaction regions (which are generated near the x-axis) form the first pulse. This will be more clearly seen later in figure 7. The outward motion of the vortex pairs reduces the magnitude of the pressure in the compression region behind the vortex pairs (that is, the compression region near the origin in figure 6*e*), and eventually the compression region is separated into two parts, as seen in figure 6(*f*). As a result, the pressure distribution around each vortex pair becomes similar to that around a single vortex ring: two rarefaction regions and two compression regions exist.

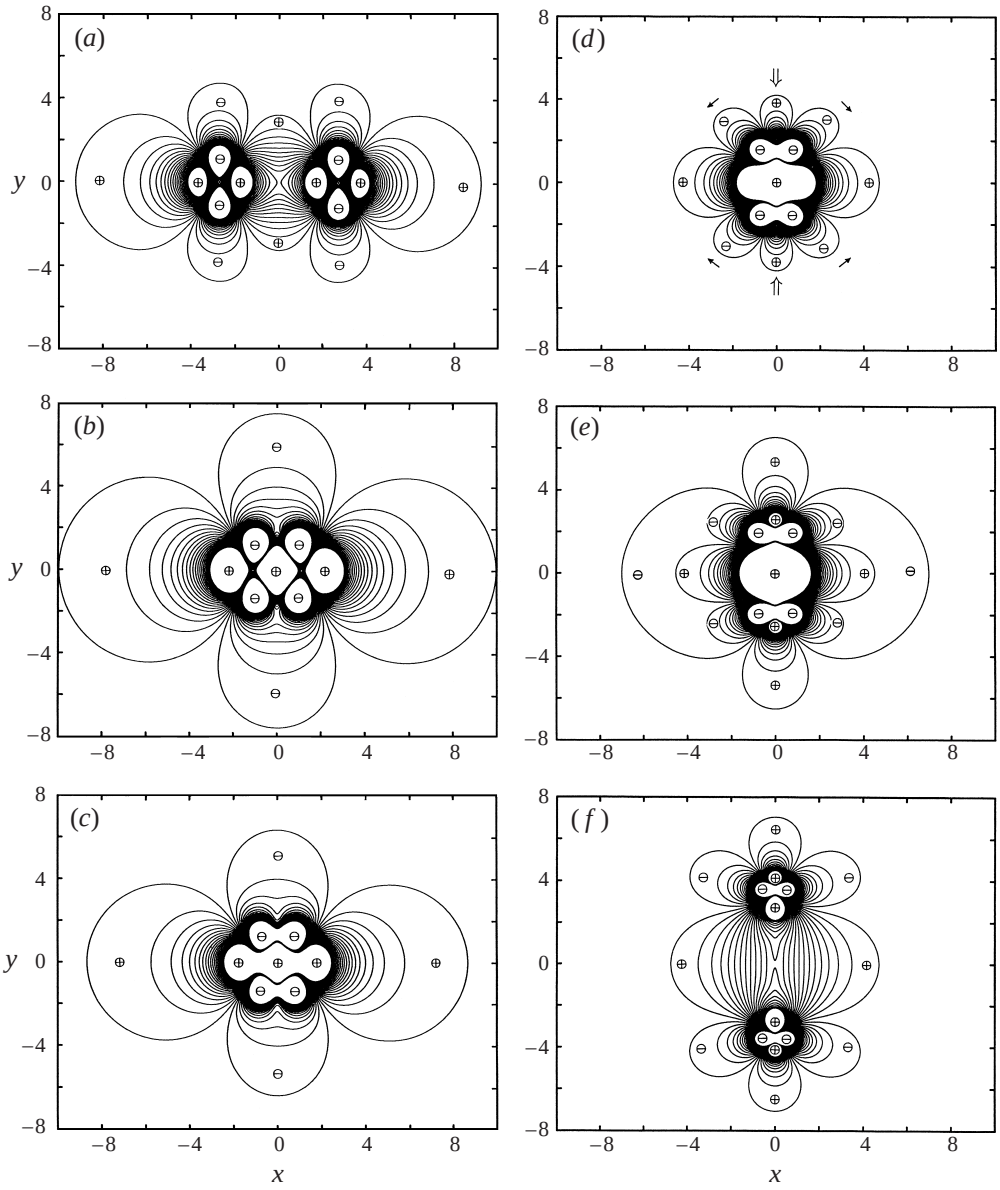

FIGURE 6. Time development of the pressure field around the vortex rings. $M_1 = M_2 = 0.15$, $r_c = 0.15$, $Re = 3300$ ($Re^* = 500$). (*a*) $t = 40$ ($t^* = 6.0$), (*b*) $t = 56$ ($t^* = 8.4$), (*c*) $t = 60$ ($t^* = 9.0$), (*d*) $t = 64$ ($t^* = 9.6$), (*e*) $t = 68$ ($t^* = 10.2$), (*f*) $t = 80$ ($t^* = 12.0$). $\Delta p_{min} = -5 \times 10^{-3}$, $\Delta p_{max} = 5 \times 10^{-3}$, with an increment of 2.5×10^{-4} for (*a*). $\Delta p_{min} = -2 \times 10^{-3}$, $\Delta p_{max} = 2 \times 10^{-3}$, with an increment of 1×10^{-4} for (*b*) to (*f*).

3.2.2. *Evolution of the pressure field in the sound region*

The magnitude of the pressure Δp decays with increasing distance from the vortex region, as will be seen later in figure 8, and in the far field it is much smaller than in the near field around the vortex rings. In order to see the transition process from the near to far fields, the evolution of the pressure field for the same flow as in figure 6 is presented in figure 7 with finer resolutions of the isobars and with wider ranges

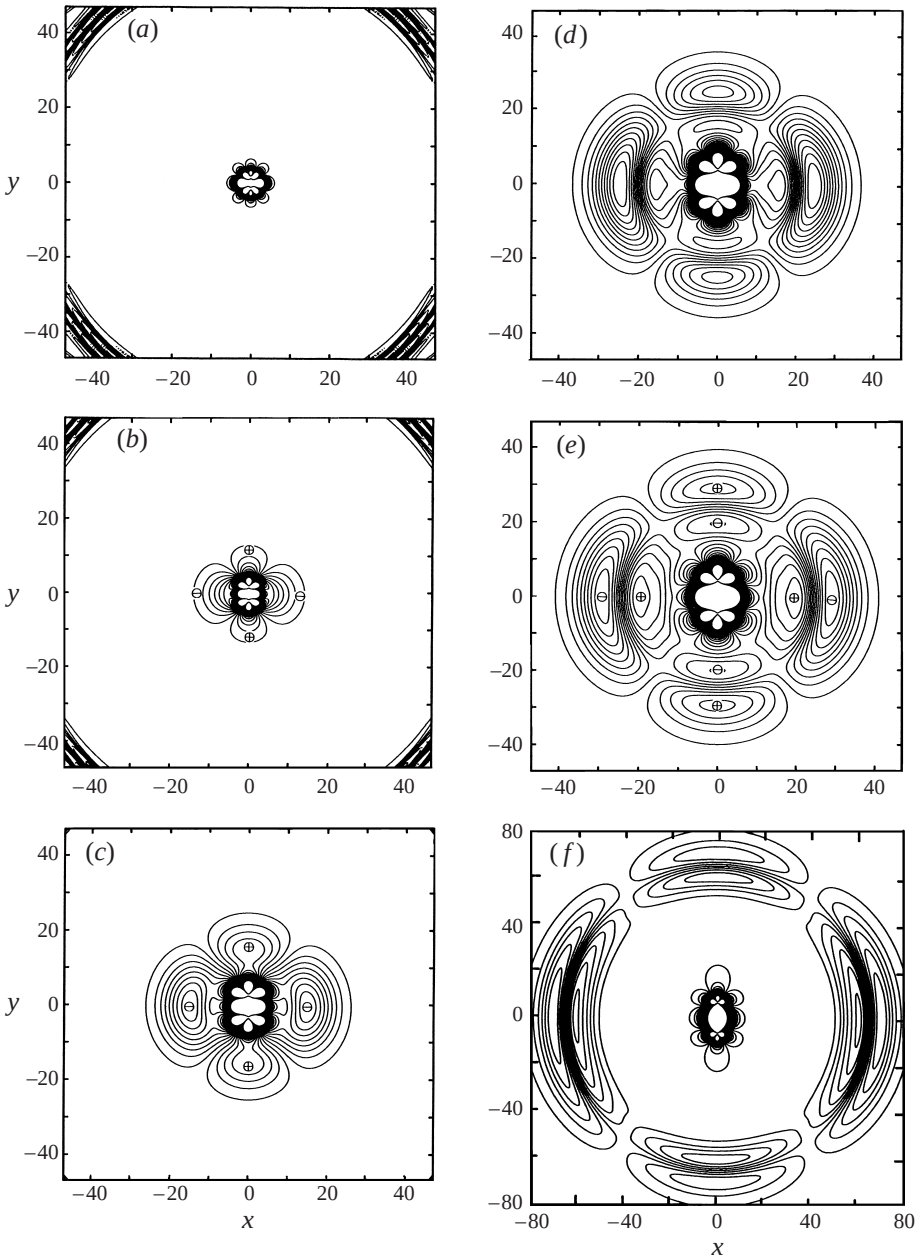

FIGURE 7. Time development of the pressure field in the sound region. $M_1 = M_2 = 0.15$, $r_c = 0.15$, $Re = 3300$ ($Re^* = 500$). (*a*) $t = 64$ ($t^* = 9.6$), (*b*) $t = 68$ ($t^* = 10.2$), (*c*) $t = 76$ ($t^* = 11.4$), (*d*) $t = 84$ ($t^* = 12.6$), (*e*) $t = 88$ ($t^* = 13.2$), (*f*) $t = 128$ ($t^* = 19.2$). $\Delta p_{min} = -2 \times 10^{-4}$, $\Delta p_{max} = 2 \times 10^{-4}$, with an increment of 1×10^{-5} for (*a*) and (*b*). $\Delta p_{min} = -5 \times 10^{-5}$, $\Delta p_{max} = 5 \times 10^{-5}$, with an increment of 2.5×10^{-6} for (*c*). $\Delta p_{min} = -2 \times 10^{-5}$, $\Delta p_{max} = 2 \times 10^{-5}$, with an increment of 1×10^{-6} for (*d*) and (*e*). $\Delta p_{min} = -1 \times 10^{-5}$, $\Delta p_{max} = 1 \times 10^{-5}$, with an increment of 5×10^{-7} for (*f*).

of the flow field ($-47 \leqslant x, y \leqslant 47$ for figures 7*a* to 7*e*, and $-80 \leqslant x, y \leqslant 80$ for 7*f*). Figures 7(*a*) and 7(*b*) show the pressure distributions at the same instants as in figures 6(*d*) and 6(*e*), respectively, but contour levels are different. As noted before in § 2.2, at an early stage of the flow development, the initial transients related to the initial

conditions are generated and propagate from the vortex rings, which are seen near the corners of figures 7(*a*) and 7(*b*). Figures 7(*a*) to 7(*c*) show that a pressure wave is generated and propagates from the vortex ring region after $t \simeq 60$. In this study, we call this pressure wave the first pulse. The circumferential variation of Δp of the first pulse is alternating, and two compression regions and two rarefaction regions appear. That is, the first pulse has a quadrupolar nature. The compression regions appear ahead of the outward moving vortex pairs and propagate toward the y-direction. The rarefaction regions appear on both sides of the vortex rings and propagate toward the x-direction. By comparing figures 7(*a*) to 7(*c*) with figures 6(*d*) and 6(*e*), and also with figures 5(*b*) and 5(*c*), we can readily see that the first pulse is generated by stretching of the vortex rings, as noted already in § 3.2.1.

Figures 7(*c*) to 7(*e*) show that a second pressure wave (hereafter referred to as the second pulse), also of quadrupolar nature, radiates after the first pulse. The circumferential pressure variation of the second pulse is opposite in sign to that of the first pulse. It should be noted that, as already seen in figure 5, the vortex rings continue to stretch after generation of the first pulse, and that no changes of direction of the vortex ring motion occur. This suggests that generation of the second pulse may not be a direct result of the change of direction of the vortex ring motion, but may come about from matching of the near and far fields, so that the harmonic constraints, $\int_{-\infty}^{\infty} \Delta p \, \mathrm{d}t = 0$ at a given point or $\int_0^{\infty} r \Delta p \, \mathrm{d}r = 0$ at a given instant, may be satisfied (Landau & Lifshitz 1987).

Figure 7(*f*) shows that appreciable pressure waves are not observed after the second pulse; that is, the number of generated pulses may be two for the case of a head-on collision.

3.3. *Decay of the sound pressure as* r^{-1}

Instantaneous distributions of the pressure, Δp, for the same flow as in figures 5 to 7 are plotted against distance r from the origin in figure 8(*a*) for $\theta = 0^\circ$ and in figure 8(*b*) for $\theta = 90^\circ$. As seen from figure 8, both the first and the second pulses propagate radially with time, and the propagation velocity of the pulses is equal to the speed of sound. If we assume that the pulses radiate from the origin ($r = 0$), the radiation time is estimated from figure 8 to be $t \simeq 60$ for the first pulse, and $t \simeq 68$ for the second pulse. The estimated time for the first pulse is approximately equal to the starting time of stretching (figure 5*b*). This result is consistent with the estimation by the contour dynamics calculation of Shariff *et al.* (1988).

It is also seen from figure 8 that the peak values of Δp of both the first and the second pulses decay with r. The peak pressure values of the first and the second pulses measured along the $\theta = 0^\circ$ line (x-axis) and along the $\theta = 90^\circ$ line (y-axis) are plotted in figure 9 for the two vortex core sizes: $r_c (\equiv R_c/R_0) = 0.15$ and 0.3. In the figure, the solid lines denote the inverse proportion to r. We can see from figure 9 that in the far field the sound pressure decays in inverse proportion to the distance r, in agreement with the theoretical prediction (Landau & Lifshitz 1987). It is also seen from figure 9 that the vortex rings with a large core size give stronger pressure peaks than those with a small core size.

3.4. *Decomposition of the sound pressure*

The sound pressure can be expressed generally as

$$\Delta p\,(r,\theta,t) = A_0(r,t) + A_1(r,t)P_1(\cos\theta) + A_2(r,t)P_2(\cos\theta) + A_3(r,t)P_3(\cos\theta) + A_4(r,t)P_4(\cos\theta) + \cdots, \quad (3.1)$$

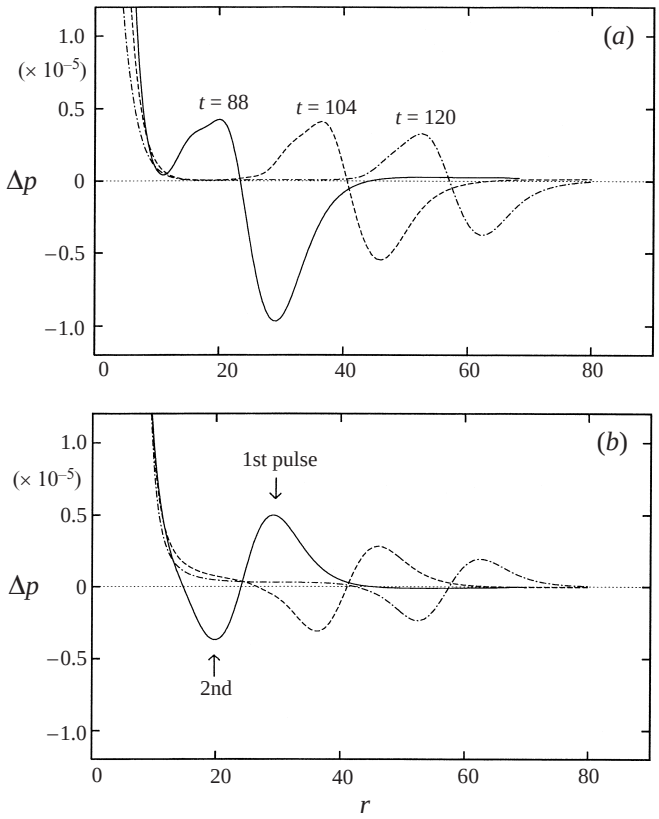

FIGURE 8. Radial distributions of the pressure, Δp. $M_1 = M_2 = 0.15$, $r_c = 0.15$, $Re = 3300$ ($Re^* = 500$). ———, $t = 88$ ($t^* = 13.2$); – – – –, $t = 104$ ($t^* = 15.6$); –•–•–, $t = 120$, ($t^* = 180$). (*a*) $\theta = 0°$, (*b*) $\theta = 90°$.

where $P_n(\cos\theta)$ are the Legendre polynomials, expressed as

$$P_1(\cos\theta) = \cos\theta, \tag{3.2}$$

$$P_2(\cos\theta) = \tfrac{3}{2}\cos^2\theta - \tfrac{1}{2}, \tag{3.3}$$

$$P_3(\cos\theta) = \tfrac{5}{2}\cos^3\theta - \tfrac{3}{2}\cos\theta, \tag{3.4}$$

$$P_4(\cos\theta) = \tfrac{35}{8}\cos^4\theta - \tfrac{15}{4}\cos^2\theta + \tfrac{3}{8}. \tag{3.5}$$

The coefficients $A_n(r,t)$ are obtained from

$$A_n(r,t) = \frac{\int \Delta p\,(r,\theta,t) P_n(\cos\theta)\sin\theta\,\mathrm{d}\theta}{\int \{P_n(\cos\theta)\}^2 \sin\theta\,\mathrm{d}\theta} \tag{3.6}$$

$$= \frac{2n+1}{2}\int \Delta p\,(r,\theta,t) P_n(\cos\theta)\sin\theta\,\mathrm{d}\theta. \tag{3.7}$$

The expression (3.1) in the limit of low Mach number and high Reynolds number was given by Kambe *et al.* (1993) for the three-dimensional oblique collision of two vortex rings. The first term on the right-hand side of (3.1) is called a monopole, the second term a dipole, the third term a quadrupole, and the fourth term an octupole.

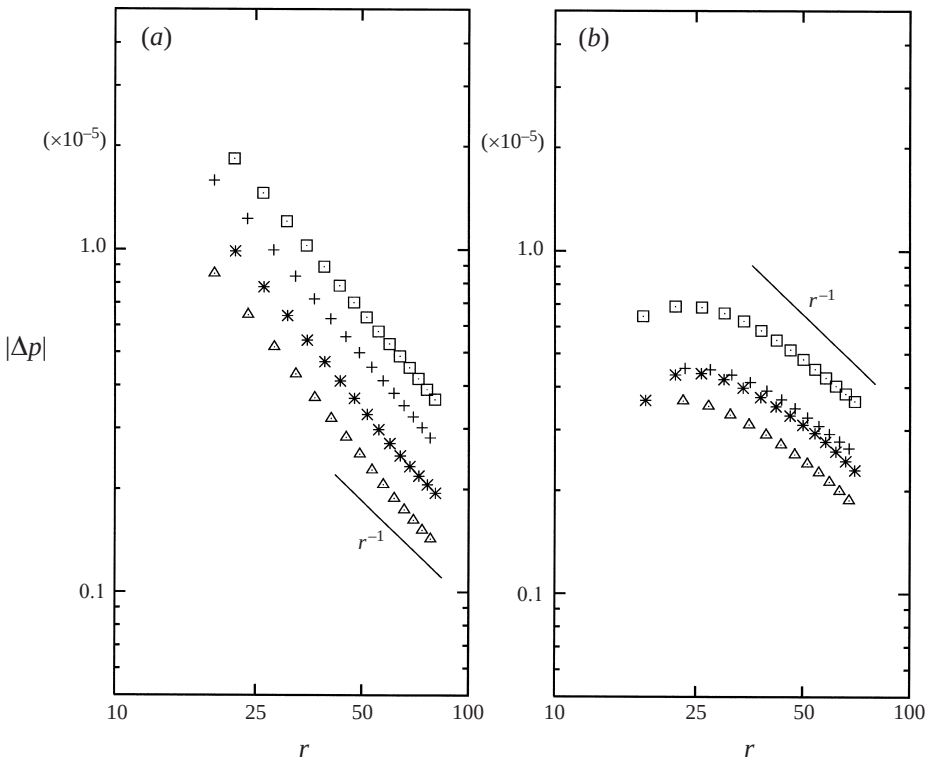

FIGURE 9. Decay of sound pressure peaks, Δp. $M_1 = M_2 = 0.15$, $Re = 3300$ ($Re^* = 500$). □, $r_c = 0.3$, $\theta = 0°$. *, $r_c = 0.3$, $\theta = 90°$. +, $r_c = 0.15$, $\theta = 0°$. Δ, $r_c = 0.15$, $\theta = 90°$. ———, $\propto r^{-1}$. (*a*) first pulse, (*b*) second pulse.

Shown in figure 10 are the first four terms of the coefficients A_n (i.e. A_0 to A_3), obtained from the present Navier–Stokes results for the case of $M_1 = M_2 = 0.15, r_c = 0.15, Re = 3300$ ($Re^* = 500$). For the case of a head-on collision, the dipole and the octupole vanish through geometrical symmetry. Therefore, as seen from figure 10, only the quadrupolar term A_2 and the monopolar term A_0 are detected. Kambe & Minota (1983) and Minota & Kambe (1986) experimentally found that the acoustic wave generated by the head-on collision of two vortex rings includes an isotropic monopolar component in addition to the quadrupolar component predicted by the inviscid theory of vortex sound. The computational result shown in figure 10 is in agreement with the experiments. Figure 10 also shows that the monopole is generated after the first peak of the quadrupole, because the monopole is related to the viscous dissipation of the kinetic energy into heat (Kambe 1984; Obermeier 1985; Minota & Kambe 1986). This result is also in agreement with the experiments.

3.5. *Wave profiles from vortex sound theory*

According to vortex sound theory, profiles of sound pressure waves may be related to the vortex ring motion. For example, let us consider the moment $I(t)$ of the source term $g(x, y, t)$ of Powell's equation (Powell 1964) which is defined as

$$I = \int \left(x^2 - \tfrac{1}{2}y^2\right) g y \, \mathrm{d}y \, \mathrm{d}x, \tag{3.8}$$

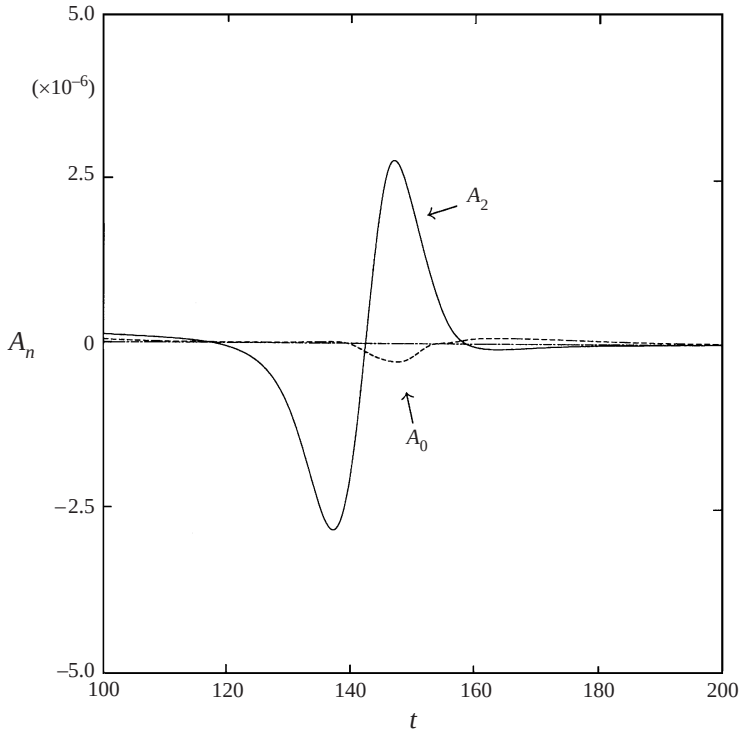

FIGURE 10. Amplitudes of wave modes. $M_1 = M_2 = 0.15$, $r_c = 0.15$, $Re = 3300$ ($Re^* = 500$). Measured at $r = 80$. – – – –, monople (A_0); · · · · ·, dipole (A_1); ———, quadrupole (A_2); –•–•–, octupole (A_3).

$$g = \nabla \cdot (\omega \times u). \tag{3.9}$$

Under the assumption of low Mach number, high Reynolds number and acoustic compactness, the moment I is related to the moment Q of the vorticity ω as (Crighton 1981)

$$I(t) = \frac{1}{2\pi}\frac{\mathrm{d}Q}{\mathrm{d}t}, \tag{3.10}$$

$$Q(t) = 2\pi \int xy^2\omega \,\mathrm{d}y\,\mathrm{d}x. \tag{3.11}$$

Using the matched asymptotic expansion, the sound pressure Δp is given by

$$\Delta p = \frac{1}{6r} I^{(2)}(t_r) P_2(\cos\theta) + \cdots, \tag{3.12}$$

where (2) denotes the second derivative with respect to the time and $t_r (\equiv t - r/c_\infty)$ is the retarded time. Therefore, the coefficient $A_2^P(r,t)$ of the quadrupolar component is expressed as

$$A_2^P(r,t) = \frac{1}{6r} I^{(2)}(t_r) + O(M^6). \tag{3.13}$$

Here, the superscript P denotes the term based on Powell's acoustic analogy. Note that the monopolar term is due to the viscous decay of energy (Kambe 1984) and that the dipolar term is $O(M^5)$. Therefore, the monopolar and dipolar components vanish identically in this analogy, if we consider terms up to $O(M^4)$. This may be

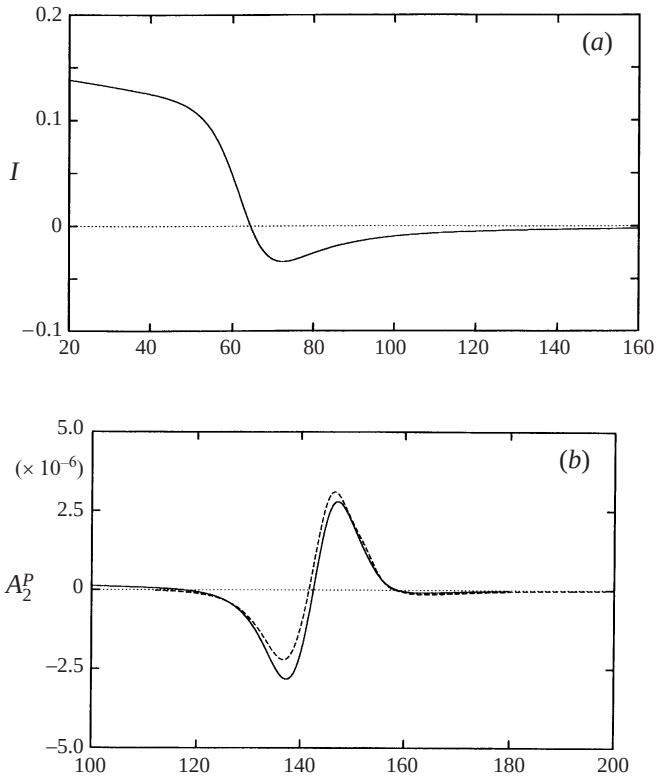

FIGURE 11. Powell's analogy. $M_1 = M_2 = 0.15$, $r_c = 0.15$, $Re = 3300$. (*a*) Moment $I(t)$, (*b*) quadrupolar component measured at $r = 80$. – – – –, A_2^P obtained by Powell's analogy; ———, A_2 obtained from DNS.

acceptable because the quadrupolar component is dominant for low Mach number flows (figure 10). As seen from (3.13), the amplitude of the quadrupolar component is proportional to the second derivative of the moment I and inversely proportional to the distance r.

The moment $I(t)$ and the quadrupolar term $A_2^P(r,t)$ measured at $r = 80$, both obtained by substituting the present DNS result into the vorticity ω of the source term $Q(t)$ in (3.11), are presented in figures 11(*a*) and 11(*b*), respectively. Figure 11(*a*) shows that at the initial stage of the flow development ($t \leqslant 50$) the moment $I(t)$ decreases gradually owing to viscous diffusion of the vortex cores. With the beginning of the interaction of the two vortex rings, $I(t)$ decreases rapidly, reaches its minimum at $t \simeq 70$ during the stretching process, and then increases and tends to vanish due to cancellation of the vorticities of the two vortex rings which have the opposite senses of rotation to each other.

The quadrupolar sound dominated by A_2^P is detected in the far field through the retarded time. In figure 11(*b*), the quadrupolar component $A_2(r,t)$ replotted from figure 10 is also presented as the solid line, for reference. We can readily see from figure 11(*b*) that A_2^P and A_2 are in good agreement. As the source term of Powell's equation vanishes where vorticity vanishes, this agreement indicates that the main source of sound is the vortex ring motion. We may also say that the vortex sound theory predicts the details of the pulses in the far field well.

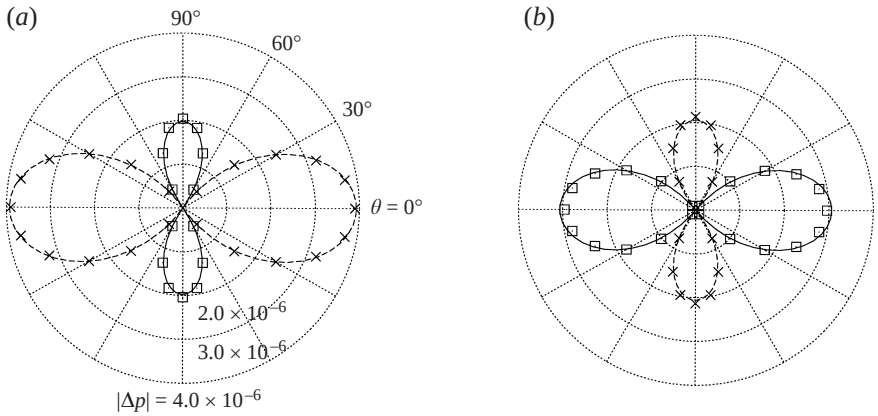

FIGURE 12. Directivity of the sound pressure. $M_1 = M_2 = 0.15$, $r_c = 0.15$, $Re = 3300$ ($Re^* = 500$). $r = 60$. (*a*) $t = 117.2$ ($t^* = 17.6$), (*b*) $t = 127.1$ ($t^* = 19.1$). □, DNS results (Δp positive); ×, DNS results (Δp negative). The solid (Δp positive) and the dashed (Δp negative) lines denote the values obtained from $\Delta p\,(r, \theta, t) = p_m(r, t) + p_q(r, t)(3\cos^2\theta - 1)$.

3.6. *Directivity of the sound pressure*

Figure 12 shows polar diagrams of the pressure distribution measured at $r = 60$ at two different instants. The radial length from the origin represents the magnitude of the pressure on a linear scale. The symbols □ and × show the present Navier–Stokes results and denote positive and negitive values of the pressure, respectively. As readily seen from the four-lobe curves in figure 12, the computational result shows the quadrupolar nature of the sounds beautifully. The directivity of the sound pressure is different for the two instants, because the first pulse arrives first at $r = 60$, figure 12(*a*), and then the second pulse follows, figure 12(*b*). Directivity similar to that in figure 12 was observed experimentally by Minota & Kambe (1986).

As noted in the previous section, for the case of head-on collision, the dipole A_1 and the octupole A_3 in (3.1) vanish from geometrical symmetry. Therefore, if we neglect terms higher than A_3, equation (3.1) can be rewritten as (Kambe & Minota 1981, 1983; Kambe 1984)

$$\Delta p\,(r, \theta, t) = p_m(r, t) + p_q(r, t)(3\cos^2\theta - 1) \tag{3.14}$$

where $p_m = A_0$ and $p_q = A_2/2$. The solid and dashed lines in figure 12 denote the values obtained by decomposing the present Navier–Stokes results, using (3.14). The solid line denotes positive values, and the dashed line denotes negative values. As readily seen from figure 12, the computational results and the results obtained from (3.14) are in good agreement, suggesting again that the sound pressure field is governed by the quadrupole and the monopole.

3.7. *Variation with $M_1(M_2)$, Re and r_c*

Kambe & Minota (1983) theoretically found that on a time scale of R_0/U_1 the following scaling law holds for the sound pressure Δp and the Mach number M_1 (or M_2) of a vortex ring:

$$\Delta p \propto M_1^4/r. \tag{3.15}$$

The experimental results of Minota & Kambe (1986) supported the validity of this scaling law. In order to confirm it numerically, the computational results for four different Mach numbers ($M_1 = 0.3, 0.15, 0.10, 0.075$) are presented in figure 13, where

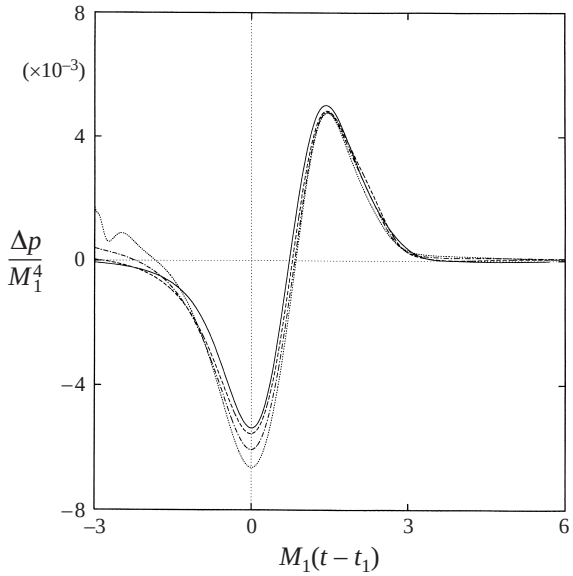

FIGURE 13. Effect of the Mach number M_1. Time histories of the normalized pressure, $\Delta p/M_1^4$, measured at $r = 80$, $\theta = 0°$. $r_c = 0.15$, $Re = 3300$. The symbol t_1 denotes the arrival time of the first pulse pressure peak at the measurement point. ———, $M_1 = 0.3$; – – – –, $M_1 = 0.15$; –•–•–, $M_1 = 0.10$; · · · · · ·, $M_1 = 0.075$.

the normalized pressure, $\Delta p/M_1^4$, is plotted against the time $t^* - t_1^* = M_1(t - t_1)$. The symbol t_1 (or t_1^*) denotes the arrival time of the pressure peak of the first pulse at the measurement point $r = 80$, $\theta = 0°$. As seen from figure 13, coincidence of the curves $\Delta p/M_1^4$ versus the time $M_1(t - t_1)$ is reasonable, supporting the validity of the scaling law for low Mach numbers. (The dependence of Δp on r^{-1} has already been confirmed in § 3.3.)

Next, in order to see the effects of the Reynolds number on the sound generation, time histories of the pressure for the case of $M_1 = M_2 = 0.15$, $r_c = 0.15$ are shown in figure 14 for four different Reynolds numbers, $Re^* = 2000, 800, 500$ and 150. We can see from the figure that the sound radiation occurs earlier and the magnitude of the pressure grows for higher Reynolds numbers. This is because loss of the translational velocity of the vortex rings due to viscous diffusion of the vortex cores decreases with decreasing viscosity; the collision (stretching) occurs earlier and the effective Mach number at the time of collision is larger for higher Reynolds numbers.

Time histories of the pressure for two different vortex core sizes, $r_c = 0.15$ and 0.3, are presented in figure 15 for the case of $M_1 = M_2 = 0.15$. In the figure, the solid line denotes the case $r_c = 0.3$, $Re = 3300$ ($Re^{**} = 2300$), the dashed line the case $r_c = 0.3$, $Re = 2660$ ($Re^{**} = 1840$), and the chain-dotted line the case $r_c = 0.15$, $Re = 3300$ ($Re^{**} = 1840$). The acoustic Reynolds number Re is the same for the solid and chain-dotted lines, while the circulation Reynolds number Re^{**} is the same for the dashed and chain-dotted lines. Figures 15 and 9 show that head-on collision of two vortex rings with larger core size gives stronger sound pressure. This is because a thinner vortex ring diffuses faster than a thicker vortex ring (Saffman 1970) and thus the effective Mach number at the time of collision is larger for thicker vortex rings.

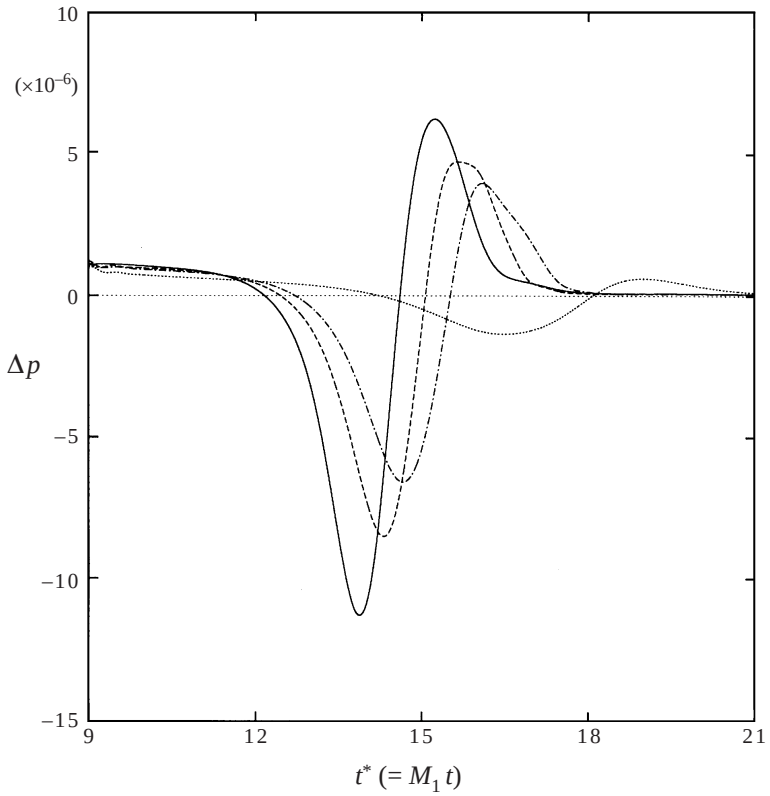

FIGURE 14. Effect of the Reynolds number. Time histories of the sound pressure, Δp, measured at $r = 40$, $\theta = 0°$. $M_1 = M_2 = 0.15$, $r_c = 0.15$. ———, $Re^* = 2000$ ($Re = 13\,300$, $Re^{**} = 7350$); – – – –, $Re^* = 800$ ($Re = 5300$, $Re^{**} = 2940$); –•–•–, $Re^* = 500$ ($Re = 3300$, $Re^{**} = 1840$); · · · · · · , $Re^* = 150$ ($Re = 1000$, $Re^{**} = 550$).

3.8. *Comparison with experiments*

Using a microphone, Minota & Kambe (1986) measured the pressure signals generated by the head-on collision of two vortex rings. The Mach number of the vortex rings was $M_1 = M_2 = 0.14$, and the Reynolds number $Re^*(= U_1 R_0/\nu_\infty)$ was 14 000. The pressure signals were measured at $r = 134$, and the signals were averaged over ten data samplings. The individual samplings showed oscillations which were not reproducible between samplings. One of the averaged pressure profiles (Data III in Minota & Kambe) is replotted in figures 16 and 17 as a solid line. In both figures, part (*a*) represents the normalized quadrupolar component $p_q(r,t)/M_1^4$ and part (*b*) represents the normalized monopolar component $p_m(r,t)/M_1^4$, both plotted against the time $t^* - t_1^* = M_1(t - t_1)$. The symbol t_1 denotes the arrival time of the pressure peak of the first pulse at the measurement point $r = 80$ in the computation and $r = 134$ in the experiment. The present computations were performed for the case of $M_1 = M_2 = 0.15$. The Reynolds numbers Re^* were 500 and 2000. Therefore, the Reynolds number in the experiment is 28 times larger than that in the computation for $Re^* = 500$, and 7 times larger than that for $Re^* = 2000$. As the vortex core size r_c was not measured in Minota & Kambe, the computational result for $r_c = 0.15$ is presented in figure 16, and that for $r_c = 0.3$ is in figure 17. In the computations, the pressure signals were measured at $r = 80$ because of the limited performance of

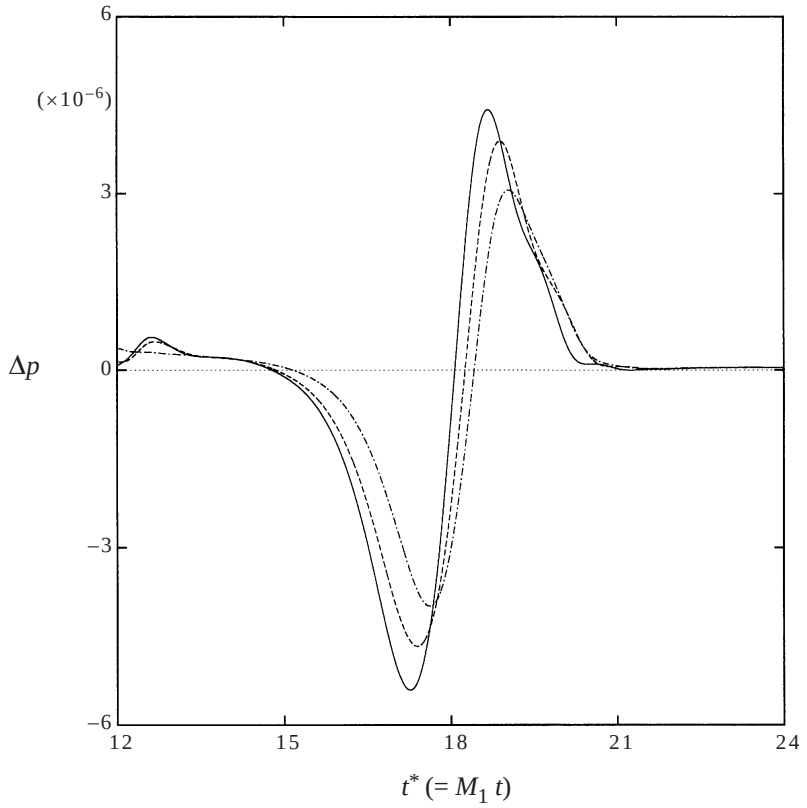

FIGURE 15. Effect of the vortex core size r_c. Time histories of the sound pressure, Δp, measured at $r = 60$, $\theta = 0°$. $M_1 = M_2 = 0.15$. ———, $r_c = 0.30$, $Re = 3300$ ($Re^{**} = 2300$); – – – –, $r_c = 0.30$, $Re = 2660$ ($Re^{**} = 1840$); –•–•–, $r_c = 0.15$, $Re = 3300$ ($Re^{**} = 1840$).

our supercomputer system. Therefore, for comparison with the computational results, the experimental pressure amplitudes measured at $r = 134$ have been converted to the values at $r = 80$ under the assumption that the sound pressure decays in inverse proportion to the distance r (figure 9).

In figures 16 and 17, we notice a few differences between the experiment and the computation. First, we can see at least four pressure peaks of the quadrupolar term in the experiment (the numbers 1 to 4 in figure 16*a*) while there are two peaks in the computation, which are the first and second pulses. At present, we have no definite explanation for this difference. One of the referees suggests that the difference would be due to the computational restriction of axisymmetry, because in reality non-axisymmetric break-down of two colliding vortices has been observed (Lim & Nickels 1992). Second, the magnitudes of the computed pressure peaks of both the quadrupole and the monopole are smaller than the experimental values. As seen from figure 16, the largest Reynolds number gives larger pressure peaks (see also figure 14). Therefore, the smaller Reynolds numbers used in the computation ($Re^* = 500, 2000$) may be responsible for the difference, at least partly. Another possible cause of the difference is that the core size r_c in the experiment might be larger than in the computation, as guessed from the comparison of the computational result for $Re^* = 500$ in figure 16 with that in figure 17 (see also figure 15). Further

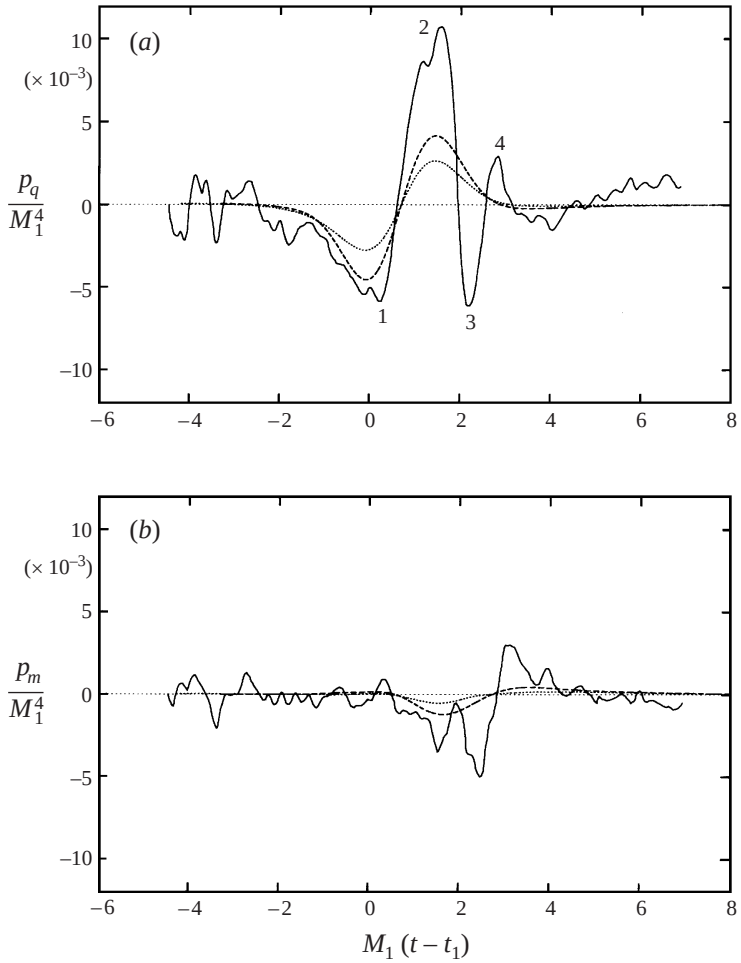

FIGURE 16. Comparison of normalized mode amplitudes with experiment. Measured at $r = 80$. – – – –, present DNS with $r_c = 0.15$, $Re^* = 2000$; · · · · · ·, present DNS with $r_c = 0.15$, $Re^* = 500$; ———, experiment by Minota & Kambe (1986) with $Re^* = 14\,000$. (*a*) Quadrupolar component (p_q/M_1^4), (*b*) monopolar component (p_m/M_1^4).

computational and experimental data should be accumulated in order to explain these differences.

Also plotted by a chain-dotted line in figure 17 is a theoretical value obtained by an extended Möhring's method. Kambe & Minota (1983) and Kambe (1984) extended Möhring's method (1978) such that the viscous effect can be taken into account. In this paper, this method is referred to as the extended Möhring's method. By this method, the monopole function $p_m(r,t)$ in (3.14) is obtained after the velocity distribution in the near field is known. Similarly, the quadrupole function $p_q(r,t)$ is obtained after the near-field vorticity distribution is known. The chain-dotted line in figure 17 was obtained from (3.14), using the present Navier–Stokes data in the vortex region as the distributions in the near field. We can see from figure 17 that the agreement between the Navier–Stokes results and the theoretical results obtained by the extended Möhring's method is satisfactory.

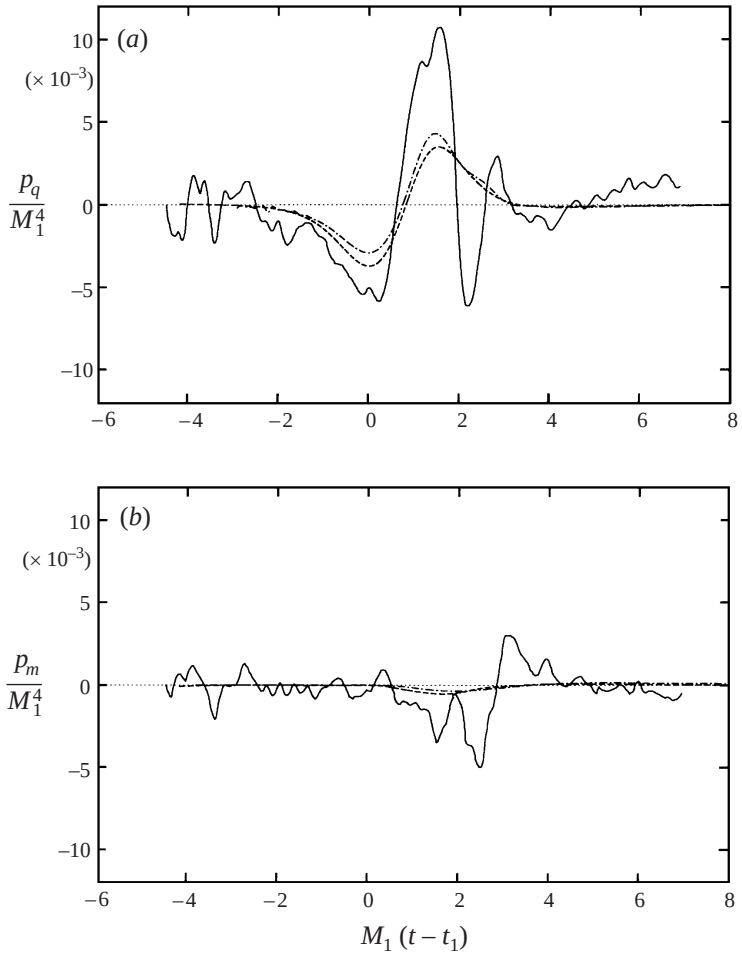

FIGURE 17. Comparison of normalized mode amplitudes with experiment and theory. Measured at $r = 80$. – – – –, present DNS with $r_c = 0.30$, $Re^* = 500$; –•–•–, extended Möhring's method with $r_c = 0.30$, $Re^* = 500$; ———, experiment by Minota & Kambe (1986) with $Re^* = 14\,000$. (*a*) Quadrupolar component (p_q/M_1^4), (*b*) monopolar component (p_m/M_1^4).

4. Results for two vortex rings of unequal strengths

In this section, computational results for the case of the collision of two vortex rings of unequal strengths (hereafter referred to as asymmetric collision) are presented. First, evolutions of the vortex ring motion and the pressure field are presented. It is shown that the generation of sound is related to the change of direction of the vortex ring motion owing to the unequal strengths. Then, the nature of the generated sound and the effects of the Mach numbers are examined. The results show that, for the case of asymmetric collision, dipolar and octupolar components appear in addition to the monopolar and the quadrupolar components which are observed for the case of head-on collision. The results also suggest that the scaling law, $\Delta p \propto M_1^4$, may hold under the condition that the Mach number ratio is the same. Then, the computational results are compared with the theoretical values predicted by the extended Möhring's method.

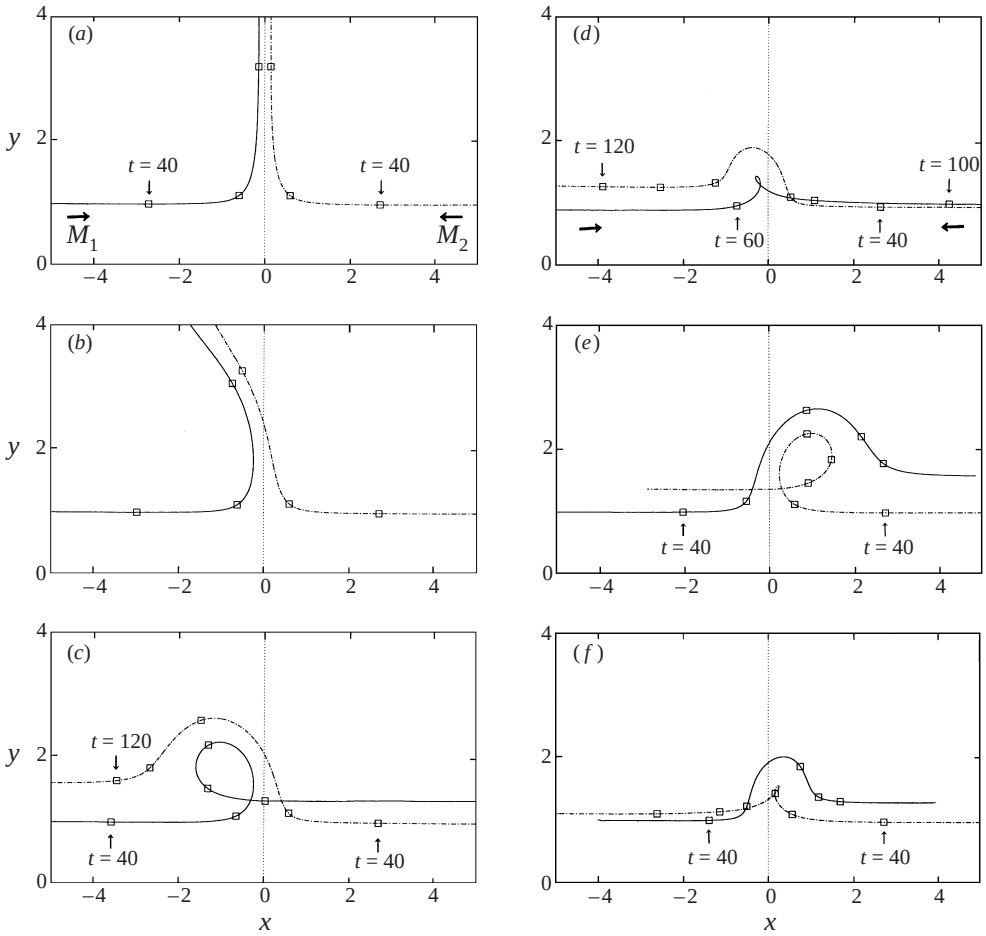

FIGURE 18. Trajectories of vortex ring centres. $M_2 = 0.15$, $r_c = 0.15$, $Re = 3300$. ———, left vortex ring; –•–•–, right vortex ring; □, location of the centre of a vortex ring at time t. The time interval between symbols (□) is 20.0. (*a*) $M_1 = 0.15$ ($M_1/M_2 = 1.0$), (*b*) $M_1 = 0.165$ ($M_1/M_2 = 1.1$), (*c*) $M_1 = 0.20$ ($M_1/M_2 = 1.33$), (*d*) $M_1 = 0.30$ ($M_1/M_2 = 2.0$), (*e*) $M_1 = 0.1125$ ($M_2/M_1 = 1.33$), (*f*) $M_1 = 0.075$ ($M_2/M_1 = 2.0$).

4.1. *Evolution of the vortex rings*

Trajectories of the centres of vortex cores in the upper half of a meridional cross-section are presented in figure 18 for various values of the Mach number M_1 of the left vortex ring with a fixed value of $M_2(= 0.15)$ of the right vortex ring. Figure 18(*a*) shows the case of head-on collision ($M_1 = M_2$), figures 18(*b*) to 18(*d*) show the cases of $M_1 > M_2$, and figures 18(*e*) and 18(*f*) show the cases of $M_1 < M_2$. The centre of a vortex core is defined as follows:

$$x_c = \frac{\iint x\omega^2 \,\mathrm{d}y\,\mathrm{d}x}{\iint \omega^2 \,\mathrm{d}y\,\mathrm{d}x}, \qquad y_c \frac{\iint y\omega \,\mathrm{d}y\,\mathrm{d}x}{\iint \omega \,\mathrm{d}y\,\mathrm{d}x}. \tag{4.1}$$

In figure 18, the solid line denotes the trajectory of the left vortex ring, and the chain-dotted line denotes that of the right vortex ring; □ denotes the instantaneous

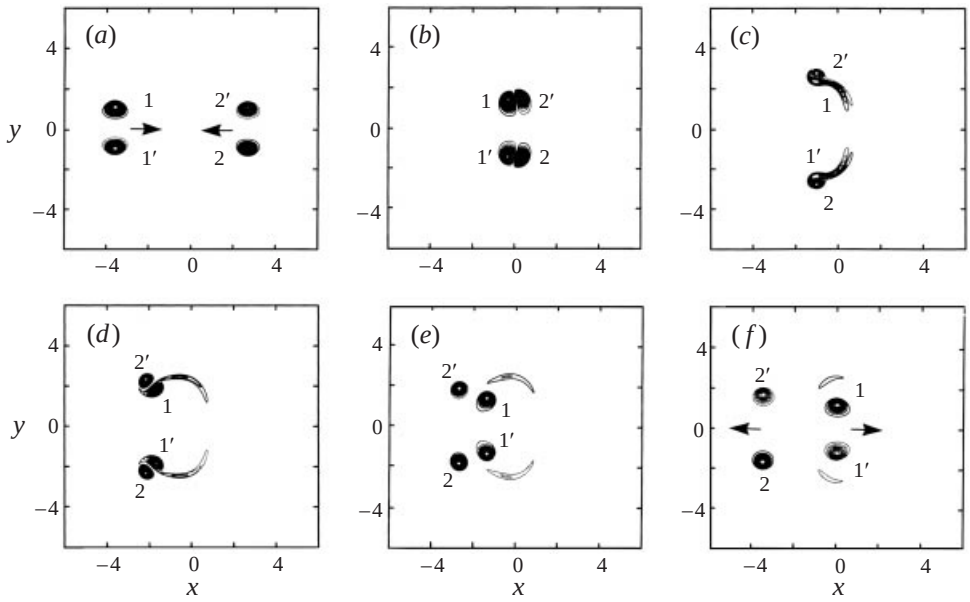

FIGURE 19. Time development of a vorticity field. $M_1 = 0.20$, $M_2 = 0.15$, $r_c = 0.15$, $Re = 3300$ ($Re^* = 667$). The contour levels are from $\omega_{min} = -3.0$ to $\omega_{max} = 3.0$ with an increment of 0.1. (*a*) $t = 40$ ($t^* = 8.0$), (*b*) $t = 64$ ($t^* = 12.8$), (*c*) $t = 76$ ($t^* = 15.2$), (*d*) $t = 88$ ($t^* = 17.6$), (*e*) $t = 100$ ($t^* = 20.0$), (*f*) $t = 120$ ($t^* = 24.0$).

location of a vortex centre, which is plotted at time intervals of 20. For the case of head-on collision, as noted in the previous section, two vortex rings approach along the x-axis, and then stretch in the y-direction (figure 18*a*). The trajectories of the two vortex rings are symmetric with respect to the ($x = 0$)-plane. When the strengths of the two vortex rings are different, as seen from figures 18(*b*) to 18(*f*), their trajectories show striking contrast. By the mutual interaction, the weaker vortex ring is induced to move outside the stronger one after the onset of stretching. On the other hand, the trajectory of the stronger vortex ring shows a loop. The radius of the loop becomes smaller with increase in the ratio of the strengths, M_1/M_2 (when $M_1 > M_2$) or M_2/M_1 (when $M_1 < M_2$), as seen from figures 18(*b*) to 18(*f*). The two vortex rings eventually pass through and move away from each other.

A typical example of asymmetric collision is presented in terms of the vorticity in figure 19 for the case of $M_1 = 0.20$, $M_2 = 0.15$, $r_c = 0.15$ and $Re = 3300$ ($Re^* = 667$). The figure shows the time development of the vorticity field in a meridional cross-section. The time is shown by t in the figure; the corresponding time t^* is presented in the caption. The numbers 1 and 2 denote the left (stronger) and right (weaker) vortex rings, respectively, and the prime denotes clockwise rotation. The two vortex rings are located initially at $x = -10.7$ and $x = 8.0$, respectively. As in the case of head-on collision (§ 3.1), the vortex ring motion can be explained in terms of the vortex pairs in a meridional cross-section. Initially, the two vortex pairs, $(1, 1')$ and $(2, 2')$, approach along the x-axis at their respective self-induced velocities (figure 19*a*). Then, in the same way as in the case of head-on collision, new vortex pairs, $(1, 2')$ and $(1', 2)$, start to move away from the x-axis at $t \sim 60$ (figure 19*b*). As the left vortex ring is stronger than the right vortex ring, the new pairs tend to move toward the negative x-direction, and the vortex rings become coplanar at $t \sim 76$ (figure 19*c*). Following Tang & Ko (1995), we call this instant the pass-through instant. After the

pass-through instant, the two vortex rings tend to shrink and their radii decrease; in the meridional cross-section, the distance between the two vortices, 1 and 1′, becomes shorter with time, and thus the mutual interaction between 1 and 1′ becomes stronger with time than those between 1 and 2′ and between 1′ and 2. As a result, the old vortex pairs, $(1, 1')$ and $(2, 2')$, revive and recover the initial directions of their motion, which are parallel to the x-axis: $(1, 1')$ moves toward the positive x-direction, while $(2, 2')$ moves toward the negative x-direction (figure 19*d–f*). Thus, in accordance with the trajectories of the vortex centres shown in figure 18(*c*) the weaker vortex ring moves outside the stronger vortex ring which shows a loop motion.

4.2. *Generation and propagation of sound waves*

4.2.1. *Evolution of the pressure field near the vortex rings*

Isobars of $\Delta p\,(= p - p_\infty)$ around the vortex rings for the same case as in figure 19 are presented in figure 20, where $\oplus$ denotes the compression regions ($\Delta p > 0$) and $\ominus$ denotes the rarefaction regions ($\Delta p < 0$). As in the case of head-on collision, at an initial stage of the flow development, four rarefaction regions and four compression regions appear in a meridional cross-section of the flow field (figure 20*a*). With increased time, the two vortex rings approach, and the compression regions ahead of them merge (figure 20*b*). Then, the two vortex rings start to stretch at $t \simeq 60$ (figure 18*c*), and the new vortex pairs in the meridional cross-section move outward, away from the x-axis (figure 19*b*). This outward motion of the vortex pairs produces new compression regions ahead of them, which are marked by open arrows in figure 20(*c*). The appearance of the new compression regions forces the rarefaction regions around the vortex pairs to move circumferentially, as shown by solid arrows in figure 20(*c*). This circumferential movement of the rarefaction regions produces new rarefaction regions outside the compression regions near the x-axis, which are seen in figure 20(*d*). This generation mechanism of the new compression and rarefaction regions is the same as that for the case of head-on collision discussed in § 3.2.1 (figure 6); the first pulse is generated in the same way as that in the case of head-on collision.

With further increased time, the two vortex rings tend to move toward the negative x-direction (figure 18*c*), and become coplanar at the pass-through instant, $t \sim 76$ (figure 19*c*). In accordance with this vortex ring motion, the compression regions ahead of the vortex pairs in the meridional cross-section move circumferentially toward the negative x-axis, which is shown by the solid arrows in figures 20(*d*) and 20(*e*). This circumferential movement of the compression regions produces a new compression wave which propagates toward the negative x-direction ($\theta = 180°$), as seen near the x-axis in figure 20(*f*). At the same time, the compression region behind the vortex pairs, which existed near the origin when the stretching started (figure 20*c*), moves toward the positive x-direction ($\theta = 0°$), resulting in the generation of a new compression wave which propagates toward the positive x-direction (figure 20*d–f*). The vortex ring motion also induces a circumferential movement of the rarefaction regions near the vortex pairs toward the y-axis (also shown by the solid arrows in figures 20*d*, *e*), and produces new rarefaction waves which are seen in figure 20(*f*), and more clearly in figure 21(*e*, *f*) shown later. These new compression and rarefaction waves form the second pulse. Thus, in the case of asymmetric collision, the second pulse is generated by the change of direction of the vortex ring motion, in contrast to the generation of the second pulse in the case of head-on collision described in § 3.2.2.

With further increase of time beyond the pass-through instant, the vortex rings start to shrink, and in the meridional cross-section the old vortex pairs tend to re-

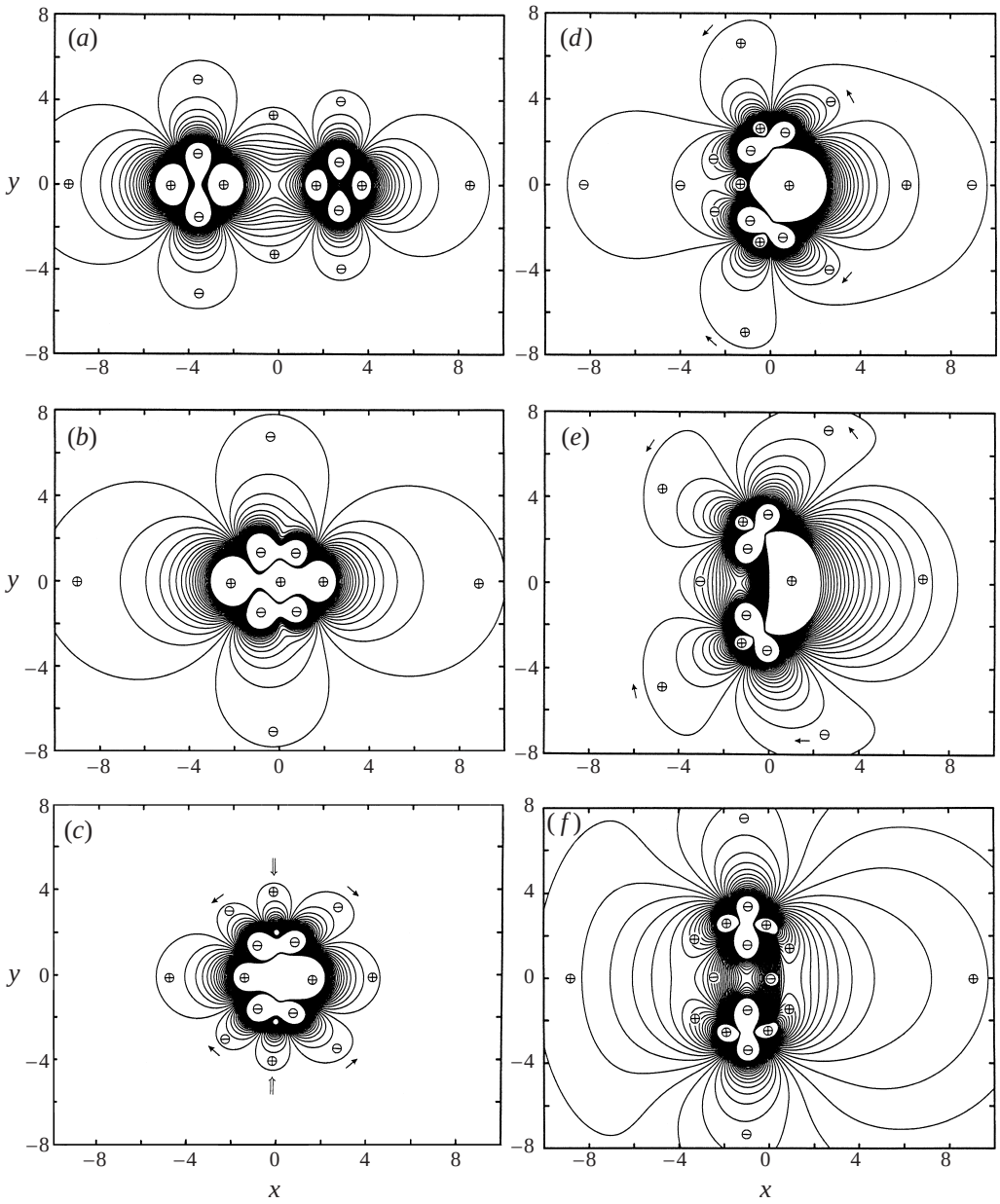

FIGURE 20(*a–f*). For caption see facing page.

vive and move toward their initial x-directions, respectively (figures 18*c* and 19*d–f*). Following the vortex ring motion, the pressure field around the vortex rings changes with time, as seen in figure 20(*g–l*). From figures 20(*g*) and 20(*h*), no new pressure waves are observed near the vortex rings by the time $t = 88$. However, as shown later in figure 21(*g*), the third pulse has already been generated by this time. The generation of the third pulse will be discussed in § 4.2.2. Accompanying the revival of the old vortex pairs, new compression regions are generated ahead of the vortex pairs, which are clearly seen, for example, in the regions

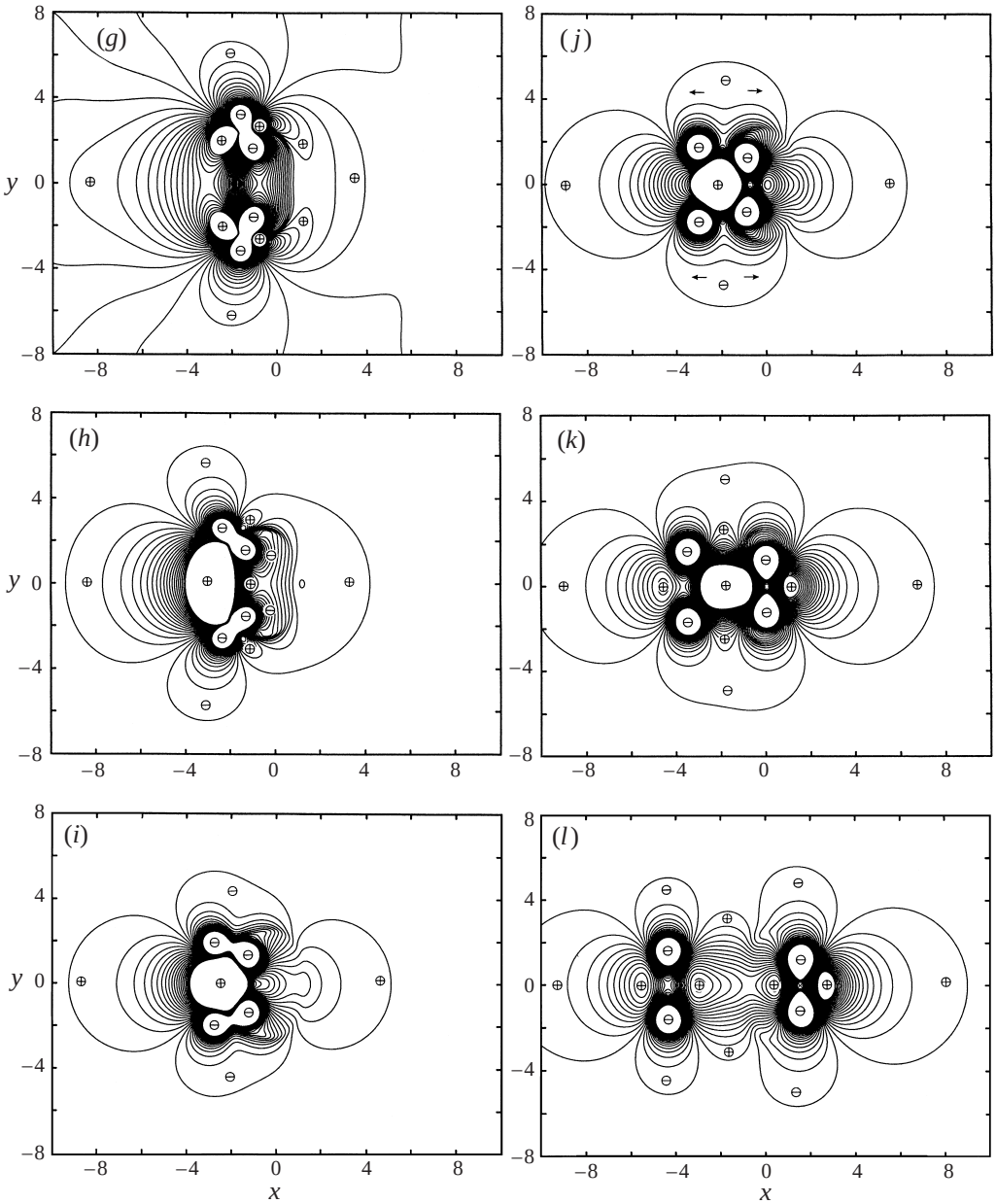

FIGURE 20. Time development of the pressure field around the vortex rings. $M_1 = 0.20$, $M_2 = 0.15$, $r_c = 0.15$, $Re = 3300$ ($Re^* = 667$). (*a*) $t = 40$ ($t^* = 8.0$), (*b*) $t = 60$ ($t^* = 12.0$), (*c*) $t = 64$ ($t^* = 12.8$), (*d*) $t = 68$ ($t^* = 13.6$), (*e*) $t = 72$ ($t^* = 14.4$), (*f*) $t = 76$ ($t^* = 15.2$), (*g*) $t = 80$ ($t^* = 16.0$), (*h*) $t = 88$ ($t^* = 17.6$), (*i*) $t = 100$ ($t^* = 20.0$), (*j*) $t = 108$ ($t^* = 21.6$), (*k*) $t = 120$ ($t^* = 24.0$), (*l*) $t = 140$ ($t^* = 28.0$). $\Delta p_{min} = -5 \times 10^{-3}$, $\Delta p_{max} = 5 \times 10^{-3}$, with an increment of 2.5×10^{-4} for (*a*). $\Delta p_{min} = -2 \times 10^{-3}$, $\Delta p_{max} = 2 \times 10^{-3}$, with an increment of 1×10^{-4} for (*b*) to (*l*).

$[-6 \leqslant x \leqslant -4, y \simeq 0]$ and $[0 \leqslant x \leqslant 2, y \simeq 0]$ in figure 20(*k*). As seen later in figures 21 and 22, the generation of the new compression regions is related to the fourth pulse.

With further increase of time, the two vortex rings move away from each other, and

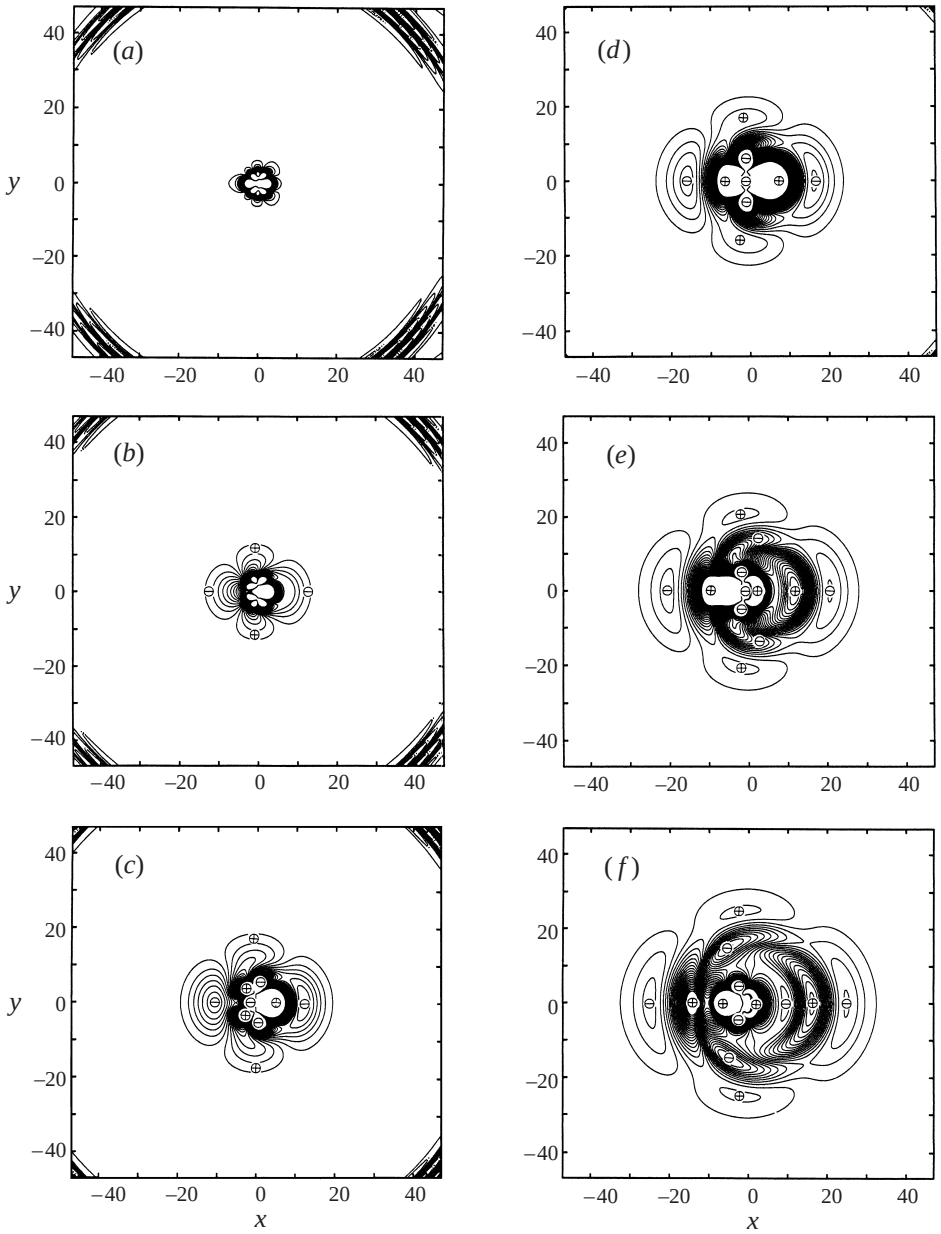

FIGURE 21 (*a–f*). For caption see facing page.

further changes of direction of the vortex ring motion were not observed; generation of additional pressure waves near the vortex rings was not observed.

4.2.2. *Evolution of the pressure field in the sound region*

The transition process of the sound pressure from the near to far fields is shown in figure 21 for the same flow as in figure 20. As readily seen by comparing figure 21(*a–c*) with figure 7(*a–c*), the generation mechanism of the first pulse for the case of asymmetric collision is essentially the same as that for the case of head-on collision:

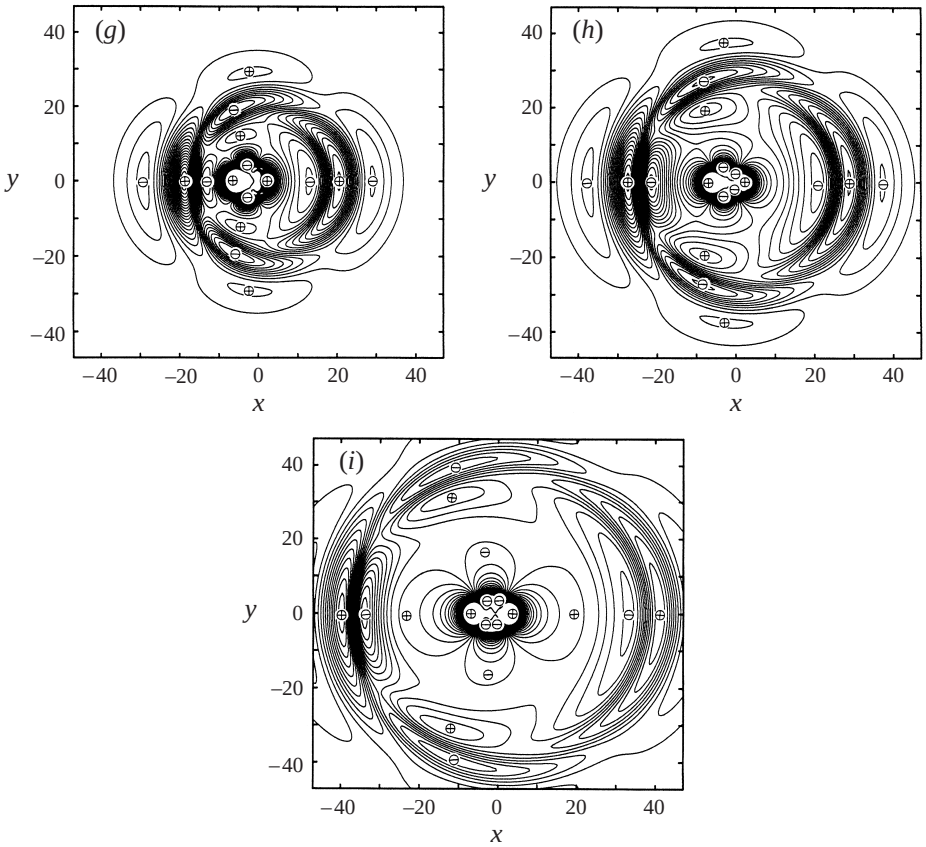

FIGURE 21. Time development of the pressure field in the sound region. $M_1 = 0.20$, $M_2 = 0.15$, $r_c = 0.15$, $Re = 3300$ ($Re^* = 667$). (*a*) $t = 64$ ($t^* = 12.8$), (*b*) $t = 68$ ($t^* = 13.6$), (*c*) $t = 72$ ($t^* = 14.4$), (*d*) $t = 76$ ($t^* = 15.2$), (*e*) $t = 80$ ($t^* = 16.0$), (*f*) $t = 84$ ($t^* = 16.8$), (*g*) $t = 88$ ($t^* = 17.6$), (*h*) $t = 96$ ($t^* = 19.2$), (*i*) $t = 108$ ($t^* = 21.6$). $\Delta p_{min} = -3 \times 10^{-4}$, $\Delta p_{max} = 3 \times 10^{-4}$, with an increment of 1.5×10^{-5} for (*a*) and (*b*), $\Delta p_{min} = -1.5 \times 10^{-4}$, $\Delta p_{max} = 1.5 \times 10^{-4}$, with an increment of 7.5×10^{-6} for (*c*) to (*e*), $\Delta p_{min} = -1.2 \times 10^{-4}$, $\Delta p_{max} = 1.2 \times 10^{-4}$, with an increment of 6.0×10^{-6} for (*f*), $\Delta p_{min} = -1.0 \times 10^{-4}$, $\Delta p_{max} = 1.0 \times 10^{-4}$, with an increment of 5.0×10^{-6} for (*g*), $\Delta p_{min} = -7.5 \times 10^{-5}$, $\Delta p_{max} = 7.5 \times 10^{-5}$, with an increment of 3.75×10^{-6} for (*h*) and (*i*).

the change of direction of the vortex ring motion from the x- to y-directions associated with stretching produces the first pulse. Figures 21(*c*) to 21(*f*), along with figures 20(*e*) to 20(*g*), suggest that the second pulse is generated by the change of direction of the vortex ring motion from y- to the negative x-directions due to the inequality of the vortex strengths.

In the positive-x region of figure 21(*f*), a new rarefaction region appears between the compression part of the second pulse and the compression region near the vortex rings; the third pulse is just being generated. The generation and propagation processes of the third pulse are clearly seen in figure 21(*g–i*). It should be noticed that Δp of the third pulse is negative near the negative x-axis, as seen from figures 21(*f*) and 21(*g*). If the third pulse is generated by the change of direction of the vortex ring motion, Δp should be positive near the negative x-axis, because the vortex pairs tend to shrink after the generation of the second pulse (figure 19*c*, *d*) and Δp ahead of the vortex pairs is positive (figure 20*g*, *h*). The generation of the third pulse is similar to

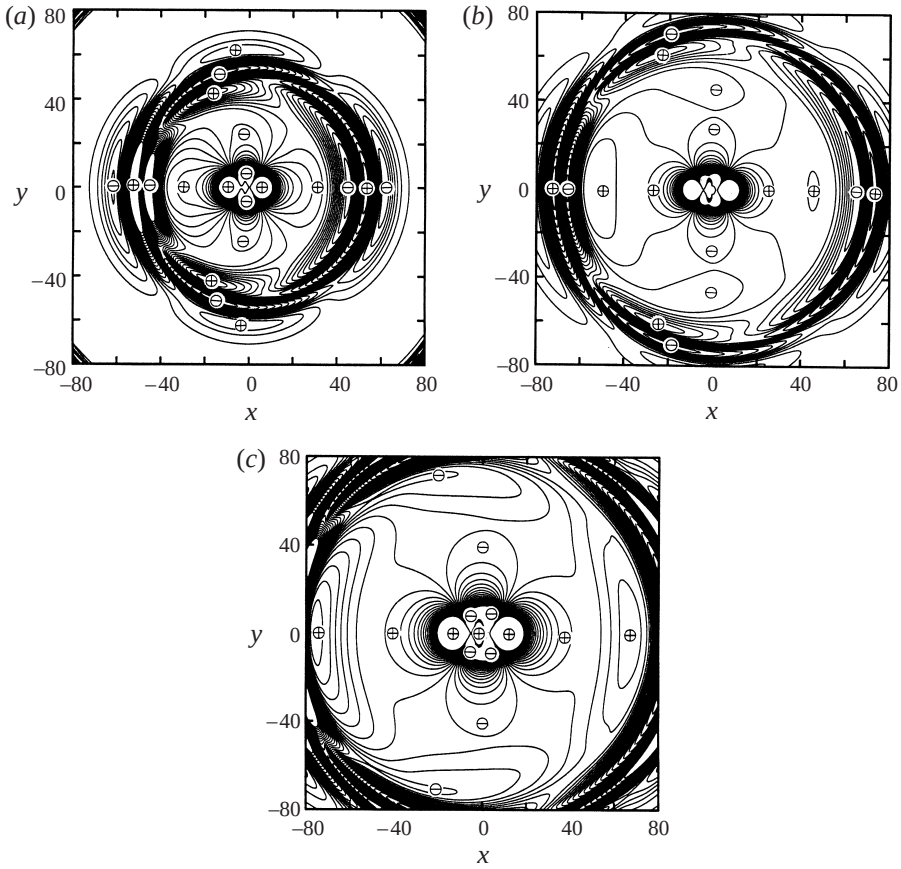

FIGURE 22. Time development of the pressure field in the sound region at later times. $M_1 = 0.20$, $M_2 = 0.15$, $r_c = 0.15$, $Re = 3300$ ($Re^* = 667$). (*a*) $t = 120$ ($t^* = 24.0$), (*b*) $t = 140$ ($t^* = 28.0$), (*c*) $t = 160$ ($t^* = 32.0$). $\Delta p_{min} = -2 \times 10^{-5}$, $\Delta p_{max} = 2 \times 10^{-5}$, with an increment of 1.0×10^{-6} for (*a*), $\Delta p_{min} = -2.2 \times 10^{-5}$, $\Delta p_{max} = 2.2 \times 10^{-5}$, with an increment of 1.1×10^{-6} for (*b*), $\Delta p_{min} = -6.0 \times 10^{-6}$, $\Delta p_{max} = 6.0 \times 10^{-6}$, with an increment of 3.0×10^{-7} for (*c*).

the generation of the second pulse in the case of head-on collision (figure 7*d*); it may not be a direct result of the change of direction of the vortex ring motion, but may come about from matching of the near and far fields.

Figure 22 shows the pressure field at later times for the same flow as in figure 21. We can see that the fourth pulse radiates from the vortex ring region. As already noted in the previous section, this is because the old vortex pairs revive and the vortex rings change their directions of motion toward their initial x-directions. Thus, in this case of $M_1 = 0.2$ and $M_2 = 0.15$, the pulses are generated four times. This is more clearly seen in figure 23 where time histories of the pressure measured at three different points ($r = 80$; $\theta = 0°$, $90°$, $180°$) are presented. In this figure, the numbers 1 to 4 denote the first to fourth pulses, respectively. As will be seen later in figure 27, the number of pulses depends on the Mach number ratio M_1/M_2. The four pulses have been confirmed to propagate radially at the speed of sound. We can also see from figure 23 that the form of the pressure wave is different for $\theta = 0°$ and $\theta = 180°$, indicating the appearance of asymmetric terms such as the dipole term $A_1(r,t)P_1(\cos\theta)$ and the octupole term $A_3(r,t)P_3(\cos\theta)$ in (3.1).

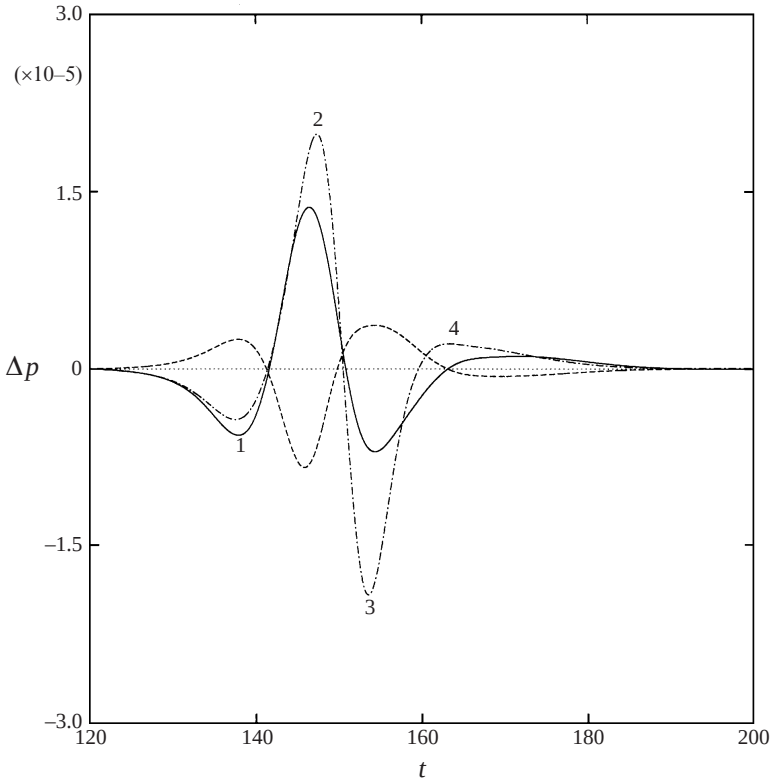

FIGURE 23. Time histories of the pressure. $M_1 = 0.20$, $M_2 = 0.15$, $r_c = 0.15$, $Re = 3300$ ($Re^* = 667$). Measured at $r = 80$. ———, $\theta = 0°$; – – – –, $\theta = 90°$; –•–•–, $\theta = 180°$.

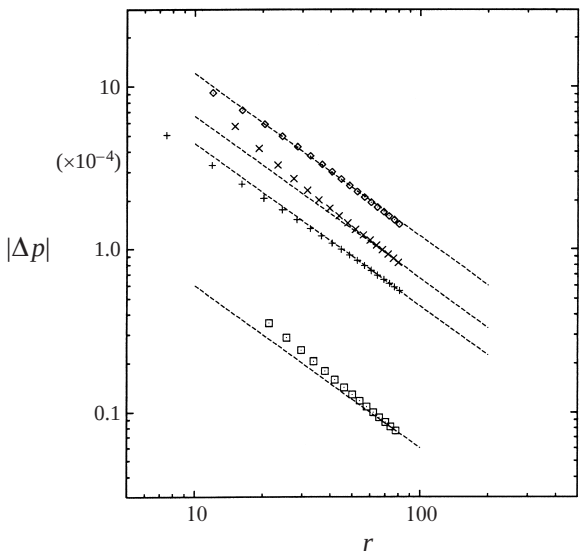

FIGURE 24. Decay of the peaks of the pressure, Δp. $M_1 = 0.3$, $M_2 = 0.15$, $r_c = 0.15$, $Re = 3300$ ($Re^* = 1000$). Measured at $\theta = 180°$. □, First pulse; ×, Second pulse; ◇, Third pulse; +, Fourth pulse; – – – –, $\propto r^{-1}$.

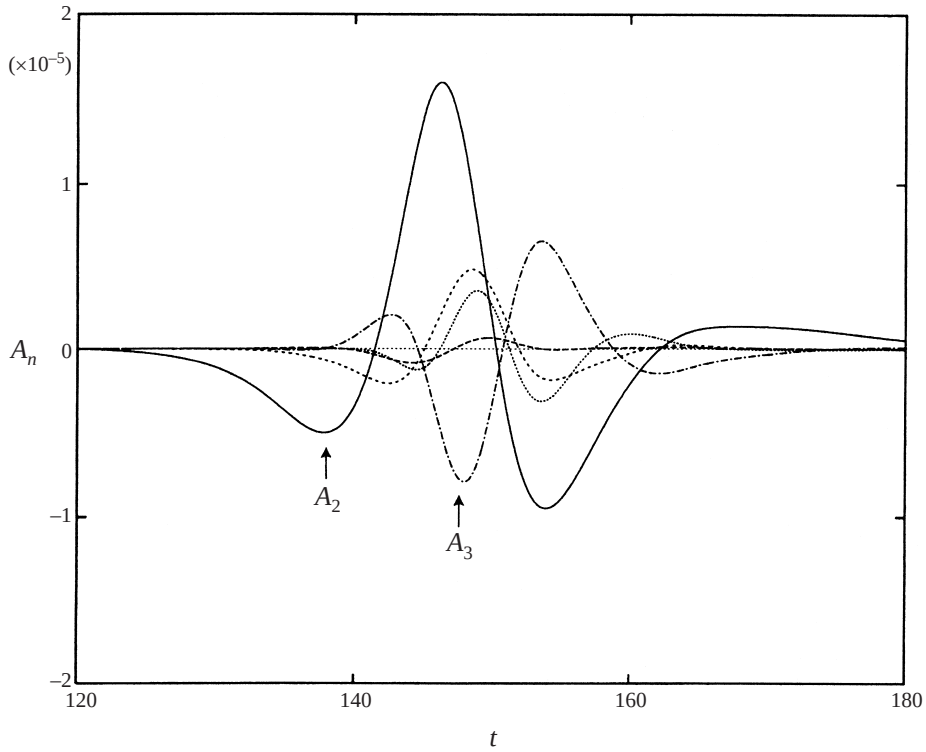

FIGURE 25. Amplitudes of wave modes measured at $r = 80$. $M_1 = 0.2$, $M_2 = 0.15$, $r_c = 0.15$, $Re = 3300$ ($Re^* = 667$). – – – –, monopole (A_0); · · · · ·, dipole (A_1); ———, quadrupole (A_2); –•–•–, octupole (A_3); ·····, (A_4).

The peak pressure values of the four pulses measured along the $\theta = 180°$ line are plotted in figure 24 for the case of $M_1 = 0.3$, $M_2 = 0.15$, $r_c = 0.15$, $Re = 3300$ ($Re^* = 1000$). From figure 24, we can see that the pressure peaks of the four pulses decay with increase in r, and reach the r^{-1}-line in the far field.

4.3. *Decomposition of the sound pressure*

As a typical result of decomposition of the sound pressure for the case of an asymmetric collision, shown in figure 25 are the first five terms of the coefficients A_n (i.e. A_0 to A_4), obtained from (3.6) using the present Navier–Stokes results for the case of $M_1 = 0.2$, $M_2 = 0.15$, $r_c = 0.15$, $Re = 3300$ ($Re^* = 667$). For the case of head-on collision, the dipolar term (A_1) and the octupolar term (A_3) vanish from geometrical symmetry, and only the quadrupolar term (A_2) and the monopolar term (A_0) are detected (figure 10). For the case of asymmetric collision, as seen from figure 25, all wave modes from A_0 to A_4 are detected. In all cases treated in this study, the magnitude of the quadrupolar term (A_2) was the largest. The amplitudes of the octupole (A_3) and the dipole (A_1) grow rapidly with growth of the inequality of the two vortex rings (that is, with increase in the Mach number ratio M_1/M_2), and in most cases A_3 was the second largest.

It should be mentioned that the dipole term (A_1) does not come from change of the total impulse. The invariance of the total impulse implies that the dipole term of $O(M^3)$ should vanish in the low Mach number limit. However, for the present case of small but finite Mach number, the octupolar terms of $O(M^5)$ give rise to a term

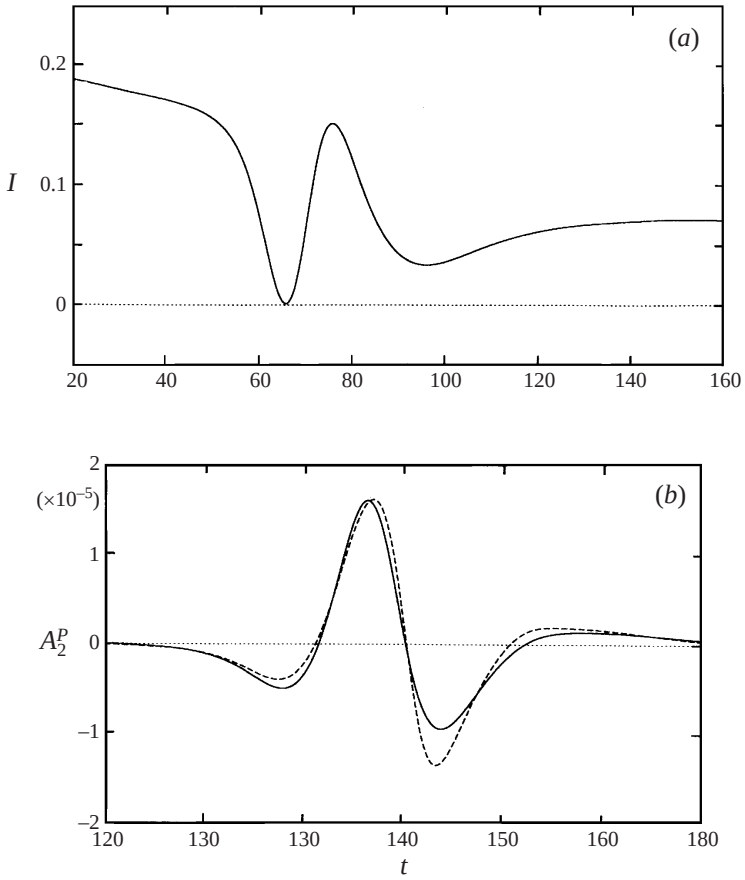

FIGURE 26. Powell's analogy. $M_1 = 0.2$, $M_2 = 0.15$, $r_c = 0.15$, $Re = 3300$. (*a*) Moment $I(t)$, (*b*) quadrupolar component measured at $r = 80$. – – – –, A_2^P obtained by Powell's analogy; ———, A_2 obtained from DNS.

proportional to $P_1(\cos\theta)$. In this sense, the dipole term $A_1(r,t)P_1(\cos\theta)$ in (3.1) may be regarded as a 'degenerate' mode of the octupolar terms.

Shown in figures 26(*a*) and 26(*b*) are the moment $I(t)$ and the quadrupolar term $A_2^P(r,t)$ measured at $r = 80$, respectively, for the same case as in figure 25. In figure 26(*b*), the quadrupolar component $A_2(r,t)$ replotted from figure 25 is also presented as the solid line, for reference. As readily seen from figure 26(*b*), A_2^P and A_2 are in good agreement, indicating again that the generation of sound is due to the vortex ring motion. Figure 26(*a*) shows that the moment $I(t)$ has three peaks: at $t \simeq 64, 76$, and 96. From the vortex motion in figure 19, we can see that the vortex rings are in the stretching process at $t \simeq 64$, close to the coplanar state at $t \simeq 76$, and are recovering their respective initial directions of motion at $t \simeq 96$.

4.4. *Variation with M_1 and M_2*

In order to see the effect of inequality of the two vortex rings, the normalized pressure, $\Delta p/M_1^4$, is plotted in figure 27 against time $t^* - t_1^* = M_1(t - t_1)$ for various values of M_1 with a fixed value of $M_2 = 0.15$. For the case of head-on collision, as shown in figure 13, the present results support the validity of the scaling law $\Delta p \propto M_1^4$. For the case of asymmetric collision, the scaling law does not hold, as readily seen from figure

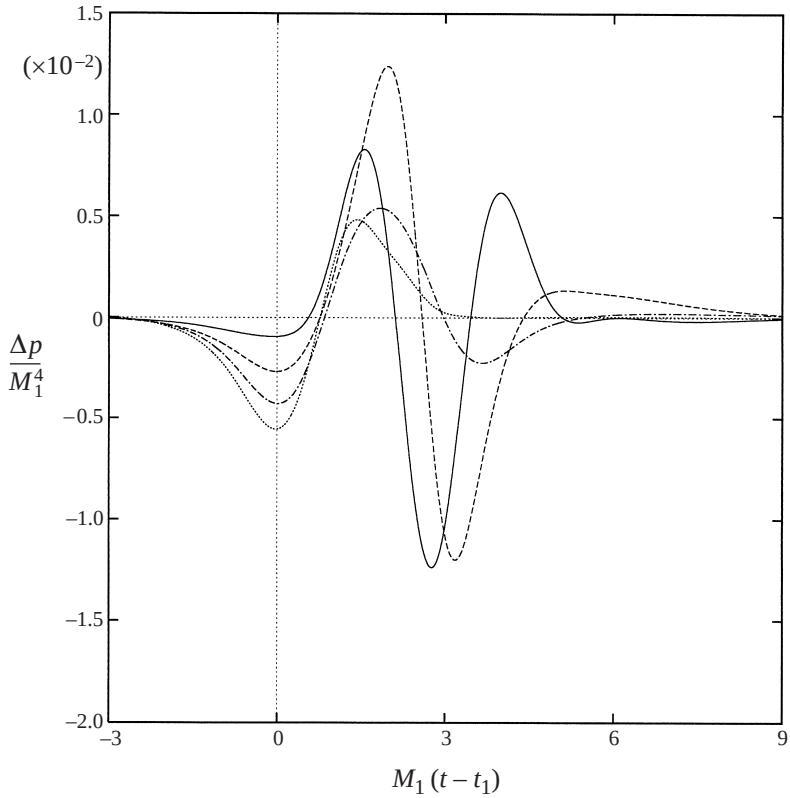

FIGURE 27. Effect of the Mach number M_1 with a fixed value of $M_2 = 0.15$. Time histories of the normalized pressure, $\Delta p/M_1^4$, measured at $r = 80$, $\theta = 180°$. $r_c = 0.15$, $Re = 3300$. ———, $M_1 = 0.3$ ($M_1/M_2 = 2.0$); – – – –, $M_1 = 0.2$ ($M_1/M_2 = 4/3$); –•–•–, $M_1 = 0.165$ ($M_1/M_2 = 1.1$); ·····, $M_1 = 0.15$ ($M_1/M_2 = 1.0$).

27. For the case of head-on collision with $M_1 = 0.15$ (dotted line in figure 27), two pressure peaks are observed which are the first and the second pulses. With increase in M_1, and thus growth of the ratio (M_1/M_2), additional pressure peaks appear.

Time histories of the normalized pressure are presented against time $t^* - t_2^* = M_1(t - t_2)$ in figure 28 for three different combinations of M_1 and M_2 with a fixed value of the Mach number ratio, $M_1/M_2 = 2$. As in figure 27, the pressure is normalized by the larger Mach number M_1. The symbol t_2 denotes the arrival time of the pressure peak of the second pulse at the measurement point $r = 80$, $\theta = 180°$. Figure 28 shows that the three curves $\Delta p/M_1^4$ versus the time $M_1(t-t_2)$ nearly coincide, suggesting the possibility that the scaling law (3.15), $\Delta p \propto M_1^4/r$, can be extended to the case of asymmetric collision, under the condition that the Mach number ratio is the same. This result is consistent with the results for trajectories of the vortex centres shown in figure 18: by comparing figure 18(*c*) ($M_1/M_2 = 4/3$) with figure 18(*e*) ($M_2/M_1 = 4/3$) or figure 18(*d*) ($M_1/M_2 = 2$) with figure 18(*f*) ($M_2/M_1 = 2$), we can see that the trajectories are similar when the Mach number ratio is the same.

4.5. *Comparison with results by the extended Möhring's method*

The sound pressure in the far field can be given by the same expression as (3.1) for a low Mach number. We obtained the coefficients A_n by the extended Möhring's method

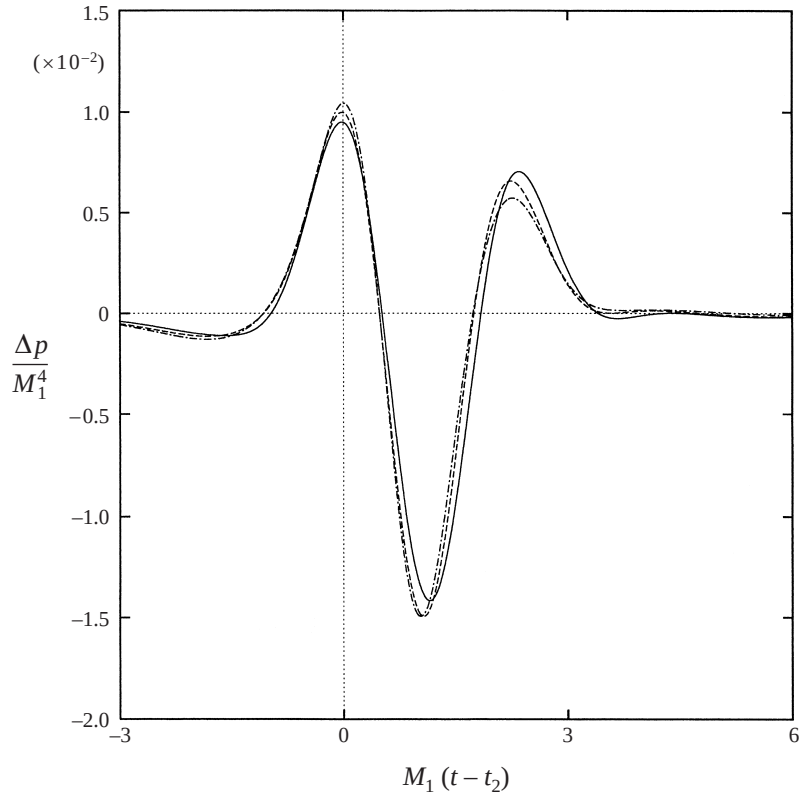

FIGURE 28. Comparison of the normalized pressure, $\Delta p/M_1^4$, at the same Mach number ratio, $M_1/M_2 = 2.0$. $r_c = 0.15$, $Re = 3300$. Measured at $r = 80$, $\theta = 180°$. t_2 denotes the arrival time of the second pulse pressure peak at the measurement point. ———, $M_1 = 0.3$, $M_2 = 0.15$; – – – –, $M_1 = 0.2$, $M_2 = 0.1$; –•–•–, $M_1 = 0.15$, $M_2 = 0.075$.

(Kambe & Minota 1983; Kambe 1984), using the present Navier–Stokes results for the vortex region as the data for the near field. Typical examples of the results obtained by the extended Möhring's method (dashed lines) are presented in figure 29 together with the DNS results (solid lines). Figure 29(*a*) shows a head-on collision; we have retained terms up to order $O(M^4)$. Figure 29(*b*) shows an asymmetric collision; we have retained terms up to $O(M^6)$, because in this case asymmetry should be included. As seen from figure 29, the extended Möhring's method gives a reasonable approximation to the Navier–Stokes results for both head-on and asymmetric collisions.

5. Conclusions

Axisymmetric, unsteady, compressible flow fields produced by the head-on collision and the asymmetric collision of two vortex rings have been studied by direct Navier–Stokes simulations over the entire region from the near to far fields. Special attention was paid to the relation between the vortex ring motion and the sound pressure waves which it generates. By illustrating the vorticity and pressure fields, the characteristic features and especially the generation and propagation processes of the sound pressure waves in the near and transition fields, which were difficult to see by conventional theoretical approaches, have been clarified in some detail.

The results show that the generation of sound is closely related to the change of

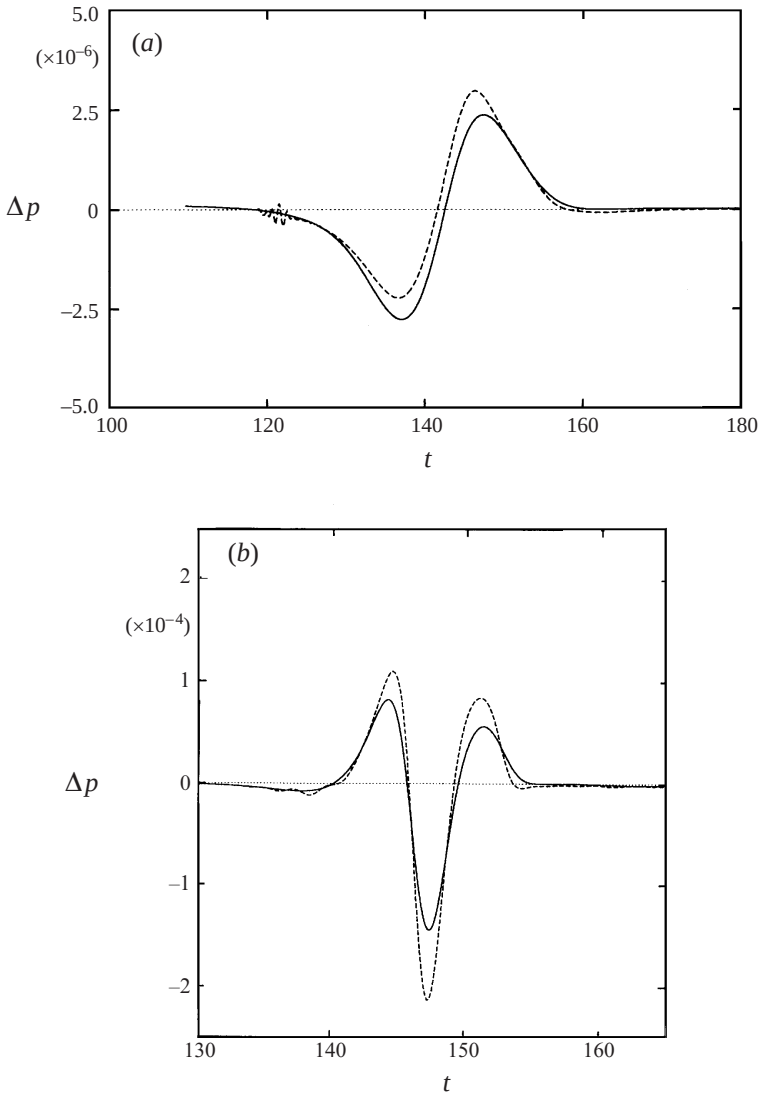

FIGURE 29. Comparison with the extended Möhring's method, Δp. $r_c = 0.15$, $Re = 3300$. Measured at $r = 80$, $\theta = 180°$. ———, present DNS; – – – –, extended Möhring's method. (*a*) Head-on collision. $M_1 = 0.15$, $M_2 = 0.15$, $Re^* = 500$. (*b*) Asymmetric collision. $M_1 = 0.3$, $M_2 = 0.15$, $Re^* = 1000$.

direction of the vortex ring motion induced by mutual interaction of the two vortex rings. Without the mutual interaction, the pressure distribution around each single vortex ring is quadrupolar in a meridional cross-section: two rarefaction regions exist around vortex cores which form a pair, and two compression regions exist ahead of and behind the vortex pair which moves at its self-induced velocity. With the mutual interaction, the two vortex pairs change their respective direction of motion and the combination of vortex cores also changes to form new vortex pairs (§ 3.1 and § 4.1). As a result, the pressure distribution in the near field changes such that the pressure ahead of and behind each vortex pair becomes or remains positive. Sound generation is related to this change of the pressure distribution in the near field.

In the case of head-on collision, the change of direction is associated with stretching

of the vortex rings. Generation of two sound pressure waves was observed. The generated pressure waves, which are called pulses in this study, consist of compression parts and rarefaction parts, and have a quadrupolar nature. The compression parts of the first pulse are generated ahead of the cores of the stretching vortex rings, and propagate toward the y-direction. The rarefaction parts of the first pulse are generated on both sides of the stretching vortex rings, and propagate toward the x-direction. The circumferential variation of the pressure distribution of the second pulse is opposite in sign to that of the first pulse. The second pulse radiates regardless of the facts that the vortex rings continue to stretch after generation of the first pulse and that no changes of direction of the vortex ring motion occur. This result suggests that the relationship between vortex ring motion and generation of sound pressure waves may not always be direct, but often comes about from matching of the near and far fields; the harmonic constraint, $\int_{-\infty}^{\infty} \Delta p \, dt = 0$ at a given point, may be satisfied.

The present results for the case of head-on collision show that the sound pressure includes an isotropic monopolar component in addition to the quadrupolar component predicted by the inviscid theory of vortex sound. This result is in agreement with the experiment of Minota & Kambe (1986). The results also support the validity of the scaling law for low Mach numbers, $\Delta p \propto M_1^4/r$, which Kambe & Minota (1983) theoretically found and the experiment of Minota & Kambe (1986) supported. On the other hand, the computation shows two pressure peaks of the quadrupolar component, while the experiment of Minota & Kambe showed at least four pressure peaks. At present, we have no definite explanation for the difference; further computational and experimental studies are required.

In the case of asymmetric collision, the two vortex rings pass through each other; the weaker vortex ring moves outside the stronger vortex ring which shows a loop motion. The vortex ring motion produces more acoustic pulses than in the case of head-on collision. The number of generated pulses depends on the relative strength of the two vortex rings (M_1/M_2). Some of the pulses (for example, the first, second and fourth pulses in figure 23) are considered to be generated directly by the change of direction of the vortex ring motion, but the other pulse (the third pulse in figure 23) is not. This result again suggests that the relationship between vortex ring motion and generation of sound pressure waves may not always be direct; some parts of the generation process of sound pressure waves are local and some are non-local.

For the case of asymmetric collision, the Mach number ratio plays an important role in sound generation: both the vortex ring motion and the pressure field depend on the ratio. The present results suggest the possibility that the scaling law, $\Delta p \propto M_1^4/r$, may be extended to the asymmetric collision case, under the condition that the Mach number ratio is the same. The present results also suggest that the sound pressure includes the dipolar and the octupolar components, in addition to the monopolar and the quadrupolar components which are observed in the case of head-on collision. The dipolar component does not come from the change of the total impulse, but appears as a degenerate mode of the octupolar components.

The study has shown that vortex sound theory predicts well the details of the pulses in the far field. Both Powell's analogy and the extended Möhring's method give a reasonable approximation to the DNS results for both head-on and asymmetric collisions, so far as the flow parameters treated in this study are concerned.

The first author expresses his sincere appreciation to Asako Inoue for her continuous encouragement. Thanks are also due to Sakari Onuma, the Institute of Fluid

Science, Tohoku University, for his technical assistance. Computations were performed on the Cray C916 at the Institute of Fluid Science, Tohoku University.

REFERENCES

Adachi, S., Ishii, K. & Kambe, T. 1997 Vortex sound associated with vortexline reconnection in oblique collision of two vortex rings. *Z. Angew. Math. Mech.* **77**, 716–719.

Colonius, T., Lele, S. K. & Moin, P. 1994 The scattering of sound waves by a vortex: numerical simulation and analytical solutions. *J. Fluid Mech.* **260**, 271–298.

Colonius, T., Lele, S. K. & Moin, P. 1997 Sound generation in a mixing layer. *J. Fluid Mech.* **330**, 375–409.

Crighton, D. G. 1981 Acoustics as a branch of fluid mechanics. *J. Fluid Mech.* **106**, 261–298.

Goldstein, M. E. 1976 *Aeroacoustics.* McGraw-Hill.

Hussain, A. K. M. F. & Zaman, K. B. M. Q. 1980 Vortex pairing in a circular jet under controlled excitation. Part 2. Coherent structure dynamics. *J. Fluid Mech.* **101**, 493–544.

Inoue, O. & Hattori, Y. 1997 Acoustic sound generated by collision of two vortex rings. *Proc. IUTAM Symp. on Dynamics of Slender Vortices*, pp. 361–368. Kluwer.

Inoue, O. & Hattori, Y. 1999 Sound generation by shock-vortex interactions. *J. Fluid Mech.* **380**, 81–116.

Ishii, K., Maru, H. & Adachi, S. 1997 Sound generation by interactions of two vortex rings. *Proc. IUTAM Symp. on Dynamics of Slender Vortices*, pp. 347–360. Kluwer.

Kambe, T. 1984 Influence of viscosity on aerodynamic sound emission in free space. *J. Sound Vib.* **95**, 351–360.

Kambe, T. & Minota, T. 1981 Sound radiation from vortex systems. *J. Sound Vib.* **74**, 61–72.

Kambe, T. & Minota, T. 1983 Acoustic wave radiated by head-on collision of two vortex rings. *Proc. R. Soc. Lond.* A **386**, 277–308.

Kambe, T., Minota, T. & Takaoka, M. 1993 Oblique collision of two vortex rings and its acoustic emission. *Phys. Rev.* E **48**, 1866–1881.

Landau, L. D. & Lifshitz, E. M. 1987 *Fluid Mechanics*, 2nd edn. Course of Theoretical Physics, Vol. 6. Pergamon.

Lele, S. K. 1992 Compact finite difference schemes with spectral-like resolution. *J. Comput. Phys.* **103**, 16–42.

Lele, S. K. 1997 Computational aeroacoustics: a review. *AIAA Paper* 97-0018.

Lim, T. T. & Nickels, T. B. 1992 Instability and reconnection in the head-on collision of two vortex rings. *Nature* **357**, 225–227.

Minota, T. & Kambe, T. 1986 Observation of acoustic emission from head-on collision of two vortex rings. *J. Sound Vib.* **111**, 51–59.

Mitchell, B. E., Lele, S. K. & Moin, P. 1995 Direct computation of the sound from a compressible co-rotating vortex pair. *J. Fluid Mech.* **285**, 181–202.

Möhring, W. 1978 On vortex sound at low Mach number. *J. Fluid Mech.* **85**, 685–691.

Moin, P. & Mahesh, K. 1998 Direct numerical simulation: a tool in turbulence research. *Ann. Rev. Fluid Mech.* **30**, 539–578.

Morse, P. M. & Feshbach, H. 1953 *Methods of Theoretical Physics.* McGraw-Hill.

Obermeier, F. 1985 Aerodynamic sound generation caused by viscous processes. *J. Sound Vib.* **99**, 111–120.

Oshima, Y. 1978 Head-on collision of two vortex rings. *J. Phys. Soc. Japan* **44**, 328–331.

Pointsot, T. & Lele, S. K. 1992 Boundary conditions for direct simulation of compressible viscous flows. *J. Comput. Phys.* **101**, 104–129.

Powell, A. 1964 Theory of vortex sound. *J. Acoust. Soc. Am.* **36**, 177–195.

Saffman, P. G. 1970 The velocity of viscous vortex rings. *Stud. Appl. Maths* **49**, 371–380.

Shariff, K. & Leonard, A. 1992 Vortex rings. *Ann. Rev. Fluid Mech.* **24**, 235–279.

Shariff, K., Leonard, A., Zabusky, N. J. & Ferziger, J. H. 1988 Acoustics and dynamics of coaxial interacting vortex rings. *Fluid Dyn. Res.* **3**, 337–343.

Sullivan, J. P., Widnall, S. E. & Ezekiel, S. 1973 Study of vortex rings using a laser Doppler velocimeter. *AIAA J.* **11**, 1384–1389.

Tam, C. K. W. 1995 Computational aeroacoustics: issues and methods. *AIAA J.* **33**, 1788–1796.

Tang, S. K. & Ko, N. W. M. 1992 Vortex interaction in unexcited coaxial jet of mean velocity ratio of 0.3. *Proc. 5th Asian Cong. Fluid Mech.* (ed. K. S. Chang & D. H. Choi), pp. 583–586.

Tang, S. K. & Ko, N. W. M. 1994 Coherent structure interaction in unexcited coaxial jet of mean velocity ratio 0.3. *Exps. Fluids* **17**, 147–157.

Tang, S. K. & Ko, N. W. M. 1995 Sound generation by a vortex ring collision. *J. Acoust. Soc. Am.* **98**, 3418–3427.

Zaman, K. B. M. Q. 1985 Far-field noise of a subsonic jet under controlled excitation. *J. Fluid Mech.* **152**, 83–111.